



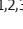
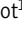



ARTICLE

Adenoviral protein E4orf4 interacts with the polarity protein Par3 to induce nuclear rupture and tumor cell death

Claire Dziengelewski^{1,2*}, Marc-Antoine Rodrigue^{1,2*}, Alexia Caillier^{1,2**}, Kévin Jacquet^{1,2**} , Marie-Chloé Boulanger⁶, Jonathan Bergeman⁴, Margit Fuchs^{1,7}, Herman Lambert^{1,2} , Patrick Laprise^{1,2,3} , Darren E. Richard^{1,3,5} , François Bordeleau^{1,2,3} , Marc-Étienne Huot^{1,2,3} , and Josée N. Lavoie^{1,2,3} 

The tumor cell-selective killing activity of the adenovirus type 2 early region 4 ORF4 (E4orf4) protein is poorly defined at the molecular level. Here, we show that the tumoricidal effect of E4orf4 is typified by changes in nuclear dynamics that depend on its interaction with the polarity protein Par3 and actomyosin contractility. Mechanistically, E4orf4 induced a high incidence of nuclear bleb formation and repetitive nuclear ruptures, which promoted nuclear efflux of E4orf4 and loss of nuclear integrity. This process was regulated by nucleocytoskeletal connections, Par3 clustering proximal to nuclear lamina folds, and retrograde movement of actin bundles that correlated with nuclear ruptures. Significantly, Par3 also regulated the incidence of spontaneous nuclear ruptures facilitated by the downmodulation of lamins. This work uncovered a novel role for Par3 in controlling the actin-dependent forces acting on the nuclear envelope to remodel nuclear shape, which might be a defining feature of tumor cells that is harnessed by E4orf4.

Introduction

The discovery of interactions between viral proteins and actin assembly machineries provides crucial information about how actin structure organization is regulated and controls cell behaviors (Delorme-Axford and Coyne, 2011; Taylor et al., 2011; Van den Broeke et al., 2014). The adenovirus (Ad) type 2 early region 4 ORF4 (E4orf4) exerts a cell-killing activity that correlates with a dramatic reorganization of actin structures and impairs cell structural integrity (Lavoie et al., 2010). Oncogenic transformation potentiates E4orf4-induced cell death, suggesting that E4orf4 targets tumor-defining features (Kleinberger, 2014; Shtrichman et al., 1999). These features should be broadly conserved in vivo, as E4orf4 can inhibit the development of various aggressive tumors in *Drosophila* without causing significant damage to healthy tissues (Rosen et al., 2019). However, the tumor cell-defining features that are targeted by E4orf4 remain elusive.

In cancer cell lines or cells transformed with viral oncogenes, the down-modulation of myosin II, which inhibits E4orf4-induced

actin remodeling, also interferes with cell death induction, therefore arguing for a role for cell contractility (Robert et al., 2006; Smadja-Lamère et al., 2008). Mechanistically, E4orf4 may affect actomyosin contractility through interactions with various signaling pathways that show mutual regulatory mechanisms, including Src kinases, PP2A- and PPI-regulatory subunits, Rho GTPases, and Hippo intermediates (Lavoie et al., 2000; Livne et al., 2001; Mui et al., 2015; Robert et al., 2006; Smadja-Lamère et al., 2008). Cellular mechanics are manipulated by E4orf4, but the clear mechanism involved is yet to be defined, as is its relevance for E4orf4-induced tumor cell killing.

Epithelial cancers characteristically deregulate cell mechanics (Mohammadi and Sahai, 2018; Zanotelli, 2018). Cancer cells often show reduced stiffness and generate more contractile forces as a result of both cellular intrinsic oncogenic alterations and microenvironment changes (Alibert et al., 2017; Kraning-Rush et al., 2012; Paszek et al., 2005). Modifications of actin

¹Centre de Recherche sur le Cancer de l'Université Laval, Québec City, Québec, Canada; ²Oncology, Centre de Recherche du CHU de Québec-Université Laval, Québec City, Québec, Canada; ³Département de Biologie Moléculaire, Biochimie Médicale et Pathologie, Université Laval, Québec City, Québec, Canada; ⁴Institut de Recherches Clinique de Montréal, Montréal, Québec, Canada; ⁵Endocrinology and Nephrology, Centre de Recherche du CHU de Québec-Université Laval, Québec City, Québec, Canada; ⁶Department of Surgery, Quebec Heart and Lung Institute/Research Center, Université Laval, Québec, Canada; ⁷Faculty of Management, Dalhousie University, Halifax, Canada.

*C. Dziengelewski and M.-A. Rodrigue contributed equally to this paper; **A. Caillier and K. Jacquet contributed equally to this paper; Correspondence to Josée N. Lavoie: josee.lavoie@crchudequebec.ulaval.ca; Marie-Chloé Boulanger's present address is Department of Surgery, Quebec Heart and Lung Institute/Research Center, Université Laval, Québec City, Québec, Canada; M. Fuchs's present address is Faculty of Management, Dalhousie University, Halifax, Nova Scotia, Canada.

© 2020 Dziengelewski et al. This article is distributed under the terms of an Attribution-Noncommercial-Share Alike-No Mirror Sites license for the first six months after the publication date (see <http://www.rupress.org/terms/>). After six months it is available under a Creative Commons License (Attribution-Noncommercial-Share Alike 4.0 International license, as described at <https://creativecommons.org/licenses/by-nc-sa/4.0/>).

subnetwork organization can contribute to mechanical deregulation and malignant cell behaviors (Denais and Lammerding, 2014; Nürnberg et al., 2011). For instance, polarity protein signaling network rewiring can promote new interactions with the actin assembly machineries that increase cell invasiveness (Gandalovičová et al., 2016; Goldstein and Macara, 2007; Halaoui and McCaffrey, 2015; Nance and Zallen, 2011). Additionally, changes in nuclear envelope (NE) protein expression, which modify nuclear shape and rigidity, influence cell metastatic potential (Alvarado-Kristensson and Rosselló, 2019; Fedorchak et al., 2014). The mechanical forces generated by contractile actin filaments are transferred to the nucleus through physical connections provided by the LINC (linker of nucleoskeleton and cytoskeleton) complex. This dynamic scaffold enables the nucleus to sense and respond to mechanical forces by modifying nuclear organization and gene expression (Friedl et al., 2011; Liu et al., 2016; Lombardi and Lammerding, 2011). How abnormal mechanical forces in tumor cells transfer signals to the nucleus is unclear.

In this study, we sought to interrogate the relevance of actomyosin contractility for E4orf4's tumor cell-selective action along with the mechanisms involved. We provide compelling evidence that E4orf4 subverts Par3 polarity protein signaling to regulate its own spatial dynamics and perturb nuclear mechanics in a tumor cell-selective manner. The data suggest that Par3 may act by the transfer of perinuclear actomyosin forces to modulate nuclear and cell shape changes. We infer that Par3 defines an important pathway to control nucleocytoplasmic coupling in tumor cells.

Results

E4orf4's tumoricidal activity is associated with actomyosin-regulated changes in nuclear shape

To determine the relevance of actomyosin changes for E4orf4's tumoricidal effect, toxicity in nontumorigenic epithelial cells and tumorigenic cell lines from various origins was initially characterized. There is currently no clear biochemical readout for E4orf4-induced cell killing, which is p53 and caspase independent in most tumorigenic cell lines tested (Landry et al., 2009; Lavoie et al., 1998; Robert et al., 2002; Shtrichman and Kleinberger, 1998). E4orf4 also modifies mitochondrial dynamics and could, therefore, impact cell metabolism before cell death (Landry et al., 2014). Thus, cytotoxicity would be better addressed by measuring cell proliferation and membrane integrity.

Clonogenic activity in breast cell lines, including nontumorigenic MCF10A cells and metastatic triple-negative MDA-MB-231 cells, was first determined after transduction of cells with recombinant Ads encoding E4orf4 or GFP as a control (Neve et al., 2006; Smadja-Lamère et al., 2008). MCF10A cells exhibited an approximately two- to fourfold higher survival rate relative to MDA-MB-231 cells after transduction at identical plaque-forming units (PFUs) per cell of Ad-E4orf4, which was associated with similar or higher E4orf4 levels in MCF10A cells, supporting a cancer cell-selective killing effect (Fig. 1 A).

To perform a robust analysis in cell lines from various origins, recombinant Ad-E4orf4-mCherry or Ad-RFP was used to

monitor the transduction efficiency microscopically. Trypan blue dye exclusion assays were performed at various times to measure cell proliferation and the percentage of dead cells within a population. Remarkably, E4orf4 had no detectable impact on cell proliferation or viability over a 3-d period in two additional nontumorigenic cell lines, HaCaT and RPE-1 cells, which were efficiently transduced (Fig. 1, B and D; and Fig. S1 A). HaCaT cells are spontaneously immortalized from adult skin keratinocytes and retain full differentiation capacity, while RPE-1 cells are near-diploid human retinal pigment epithelial cells immortalized with human telomerase reverse transcriptase (hTERT; Bodnar et al., 1998; Boukamp et al., 1988). In marked contrast, E4orf4 reduced cell proliferation in several types of cancer cell lines, including triple-negative breast cancer cells with epithelial or mesenchymal properties (MDA-MB-468 and MDA-MB-231, respectively; Bergeman et al., 2016), human bone osteosarcoma epithelial cells (U2OS), prostate carcinoma epithelial cells (22Rv1), and cervix carcinoma epithelial cells (HeLa; Fig. 1 B, Proliferation). Cancer cell lines also displayed significant increases in cell death rates at all time points, even those displaying lower transduction efficiencies (HeLa and U2OS cells; Fig. 1, C and D; and Fig. S1 A, Cell death). These results indicate that tumorigenic cells from various origins are sensitized to E4orf4-induced cell killing.

Next, E4orf4-induced morphological phenotypes and their dependence on actomyosin contractility were analyzed. Nontumorigenic epithelial cells expressing E4orf4-mCherry displayed little changes in actin cytoskeleton organization and no significant increase in cell blebbing or nuclear condensation compared with control cells expressing RFP (Figs. 2 A and S2 B; MCF10A, HaCaT, and RPE-1). In contrast, all cancer cell populations exhibited increased rates of cell blebbing and nuclear condensation in response to E4orf4 (Fig. 2 A; and Fig. S1, B and C), in line with our previous findings (Robert et al., 2006). Both phenotypes were severely blocked by blebbistatin, which downmodulates actomyosin contractility through the inhibition of myosin II (Straight et al., 2003). Furthermore, blebbistatin increased the nuclear-to-cytoplasmic ratio of E4orf4 in breast cancer cells (MDA-MB-468) without perturbing E4orf4 localization in nontumorigenic MCF10A cells (Fig. 2 B). These results imply that the regulation of E4orf4's tumoricidal activity is dependent on actomyosin contractility.

It was further observed that E4orf4-responsive cells accumulated robust actin bundles proximal to their nucleus that correlated with pronounced nuclear deformation (Fig. 2 C; compare x-z views). Quantification of nuclear circularity in lamin A/C-labeled cells clearly revealed a tumor cell-selective effect. E4orf4-induced nuclear dysmorphia, visible before the onset of cell blebbing, was characterized by striking disorganization of the nuclear lamina (Figs. 2 D and S1 C). Nuclear dysmorphia was also reduced by cell treatment with blebbistatin. These results argue that actin remodeling may cause nuclear compression. In line with this, E4orf4-expressing cells often accumulated lamin A/C at NE sites that were codistributed with apical actin fibers (Fig. 2 D, magenta arrowheads), forming lamina folds that are typical of mechanical compression (Lele et al., 2018). These results indicate that E4orf4 tumoricidal

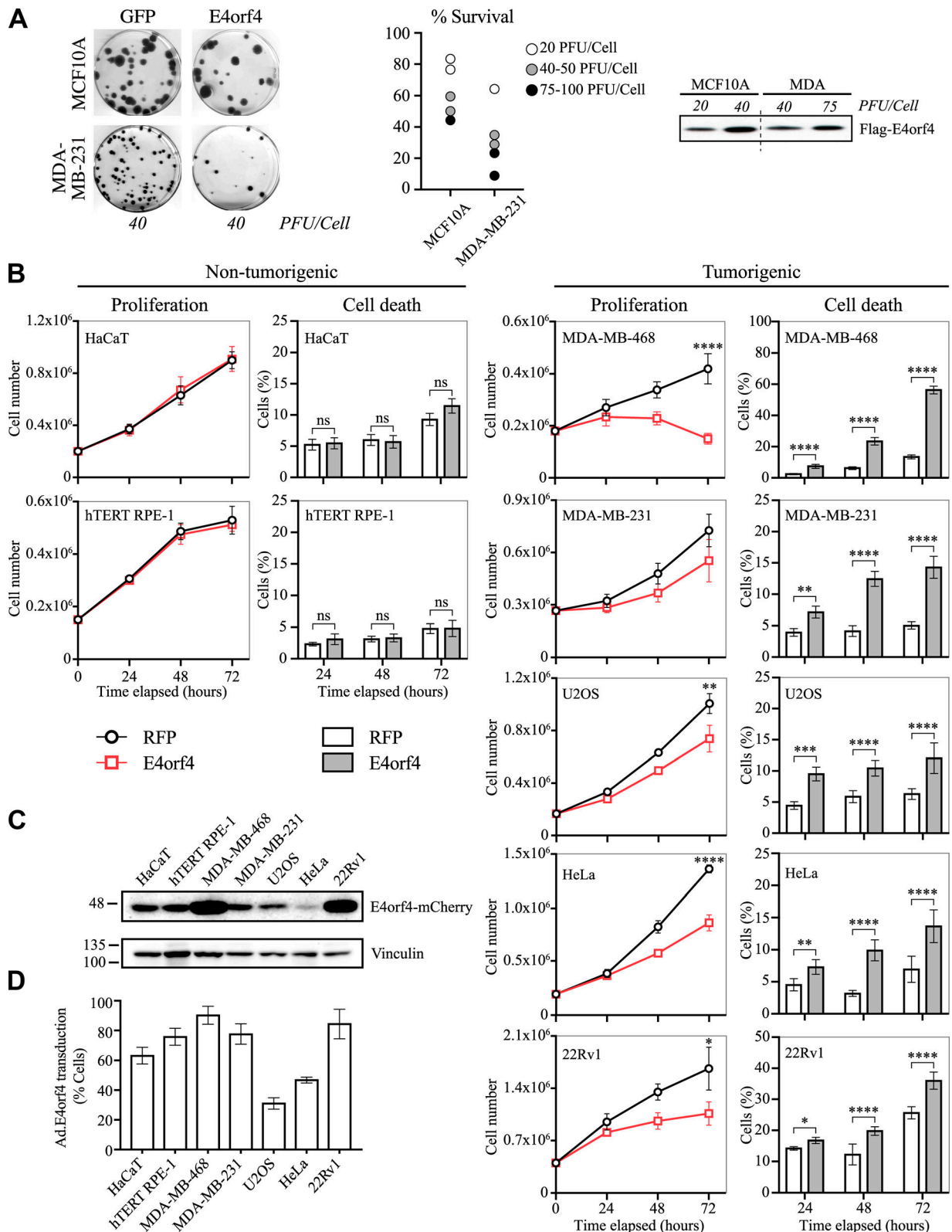


Figure 1. **Tumorigenic cells are sensitized to E4orf4's cytotoxicity.** (A) The clonogenic activity of MCF10A cells and MDA-MB-231 cells transduced with varying PFUs/cell of Ad-Flag-E4orf4. The scatterplot represents the percentage of surviving cells relative to the total number of colonies obtained in cells transduced with GFP as control (means of three technical replicates for independent biological samples). Representative IB of Flag-E4orf4 levels analyzed 48 h after transduction. (B) Graphs showing proliferation and cell death rates of nontumorigenic cell lines (HaCaT and RPE-1) compared with tumorigenic cell lines (right) at various times after transduction of Ad-E4orf4-mCherry (75 PFUs/cell) or Ad-RFP (15 PFUs/cell), as measured by Trypan blue exclusion; measurements of cell proliferation consider only viable cells, while cell death rates represent the percentage of Trypan blue-stained cells relative to the total numbers of cells.

Data are the means \pm SEM ($n \geq 3$); *, $P < 0.05$; **, $P < 0.01$; ***, $P < 0.001$; ****, $P < 0.0001$; ns, not significant. **(C)** Representative IB of E4orf4-mCherry levels assessed 48 h after transduction. **(D)** The percentage of cells expressing E4orf4-mCherry relative to the total number of infected cells, as assessed by fluorescence microscopy 48 h after transduction. See also Fig. S1 A.

activity correlates with actomyosin-driven changes in nuclear shape.

E4orf4 interacts with Par complex proteins and promotes epithelial cell polarity

We then sought to identify E4orf4 partner proteins that could regulate actomyosin dynamics. To this end, affinity purification coupled to mass spectrometry (AP-MS) was performed using breast cancer MDA-MB-231 cells that display high transduction efficiency and cell blebbing rates. Cells were transduced with a control Ad (Ad-LacZ) or an Ad encoding E4orf4 (Ad-Flag-E4orf4), and E4orf4 immune complexes were purified and processed for liquid chromatography coupled to tandem mass spectrometry (LC-MS/MS). We combined the data from three different experiments in order to perform a significance analysis of interactome (SAINT) using a stringent threshold of 0.98 (Choi et al., 2011, 2012). Among five high-confidence interactions, which include previously identified interactors (PP2A subunits; Marcellus et al., 2000; Shtrichman and Kleinberger, 1998), we selected Par3 (PARD3; Fig. 3 A) for functional analyses, based on the role of Par polarity proteins in the spatial control of actin dynamics (Goldstein and Macara, 2007; Nance and Zallen, 2011). While Par3 was previously reported as an E4orf4 partner, the relevance of this interaction has not been addressed (Mui et al., 2015).

Coimmunoprecipitation (IP) studies revealed that E4orf4 interacts with the three isoforms of Par3 in various tumorigenic cell lines, along with other Par complex proteins (Par6 and PKC ι) that are recruited by the Par3 signaling scaffold (Fig. 3, B and C, arrows; and Figs. S2 A and 4 B). Downmodulation of Par3 in 293T-shPar3 cells, which stably express a Par3-specific shRNA (293T-shRNAPar3; Fig. S2 D), reduced coprecipitation of Par6 and PKC ι , while the complex was reconstituted by introducing GFP-Par3, but not GFP (Fig. 3 C; anti-Flag E4orf4 IP). Interactions between E4orf4 and Par complex proteins were also detected in nontumorigenic MCF10A cells (Fig. 3 D). However, the ensuing impact on cell morphodynamics may depend on the cellular context, which could shape interactions between polarity proteins and the actin assembly machineries (Halaoui and McCaffrey, 2015).

Because of Par3's role in epithelial cell polarity, we examined the impact of E4orf4 in MCF10A cells that are proficient in assembling cadherin-containing adherent junctions but defective in the assembly of ZO-1-containing tight junctions (Fogg et al., 2005; Ooshio et al., 2007; Xue et al., 2013). MCF10A cells were transduced with Ad-LacZ or Ad-E4orf4 at low confluency and grown after confluency in 2D monolayers (Fig. 3 E). Cellular junction assembly was monitored after 3 and 6 d by confocal microscopy, after E-cadherin and ZO-1 immunostaining. Remarkably, E4orf4-expressing cells exhibited a more rapid expansion of E-cadherin-labeled adherent junctions at day 3, as revealed by the significant increase in cortical E-cadherin

staining (Fig. 3, F and G). Moreover, we observed the presence of E4orf4-expressing cells in which ZO-1 staining showed a more contiguous apical staining that contrasted with the fragmented and cytoplasmic staining of ZO-1 in control cells (Fig. 3 H, y-z views; magenta arrows). These results suggest that E4orf4 promotes assembly of cell-cell junctions in nontumorigenic epithelial cells rather than cell blebbing and death, as widely observed in cancer cells.

E4orf4's interaction with Par3 enables the corruption of actomyosin dynamics in tumorigenic cells

In the context of cancer cells, Par3 has both tumor-suppressive and tumor-promoting functions, of which the latter would involve its scaffolding function (Iden et al., 2012). A crucial role for Par3 now emerges in the segregation of actomyosin structures (Mack and Georgiou, 2014; Munro, 2017). Thus, we hypothesized that subversion of Par3's scaffolding function by E4orf4 contributes to its tumoricidal effect on cell mechanics.

To test this hypothesis, the structural requirements for E4orf4-Par3 interaction were first characterized. We found that Par3 binding was mediated by a conserved motif across Ad serotypes, proximal to a K88 residue previously shown to impact the E4orf4-Par3 interaction (Fig. 4 A; Mui et al., 2015). Substitution of a single negatively charged residue (D90A) reduced binding, while modification of three residues (DYV to GGG, to minimize structural alteration) blocked Par3 binding without impairing interaction with PP2A (Fig. 4 B). Conversely, an E4orf4 construct that is defective in PP2A binding (F84A) was able to interact with Par3, indicating that these interactions are independent (Fig. 4 B; Champagne et al., 2004; Marcellus et al., 2000). To identify the E4orf4-binding domain on Par3, we performed IP studies in 293T-shPar3 cells after transfection of E4orf4 and GFP-Par3 constructs that contain deletions of key functional domains, including the oligomerization domain (Δ Nter), Par6-binding domain (Δ PDZ), a protein kinase C-binding domain (Δ PKC-BD), or the C-terminal domain (Δ Cter; Fig. S2, B-D). Only GFP-Par3 (Δ Cter) showed a significant binding loss after reciprocal IPs (Fig. S2, E and F). These results agreed with findings in Fig. 3 showing that E4orf4 can associate with PKC ι and Par6 via Par3.

We then sought to visualize the in situ subcellular interaction of E4orf4 and Par3 by performing a Duolink proximity ligation assay (PLA) in HeLa cells. Numerous fluorescent foci were detected in HeLa cells expressing WT E4orf4, which were enriched proximal to important nuclear deformations (Fig. 4, C and D, WT; and Fig. S3 A). Foci numbers were decreased by \sim 85% in cells expressing E4orf4 (GGG), corroborating the importance of a loss of Par3 binding (Fig. 4 D). Phosphorylated PKC substrates were also detected at sites of nuclear deformation that would indicate major sites of E4orf4-Par3 interaction (Fig. S3 B). Intriguingly, loss of Par3 binding led to an approximately two- to threefold increase in the nuclear-to-cytoplasmic ratio of E4orf4,

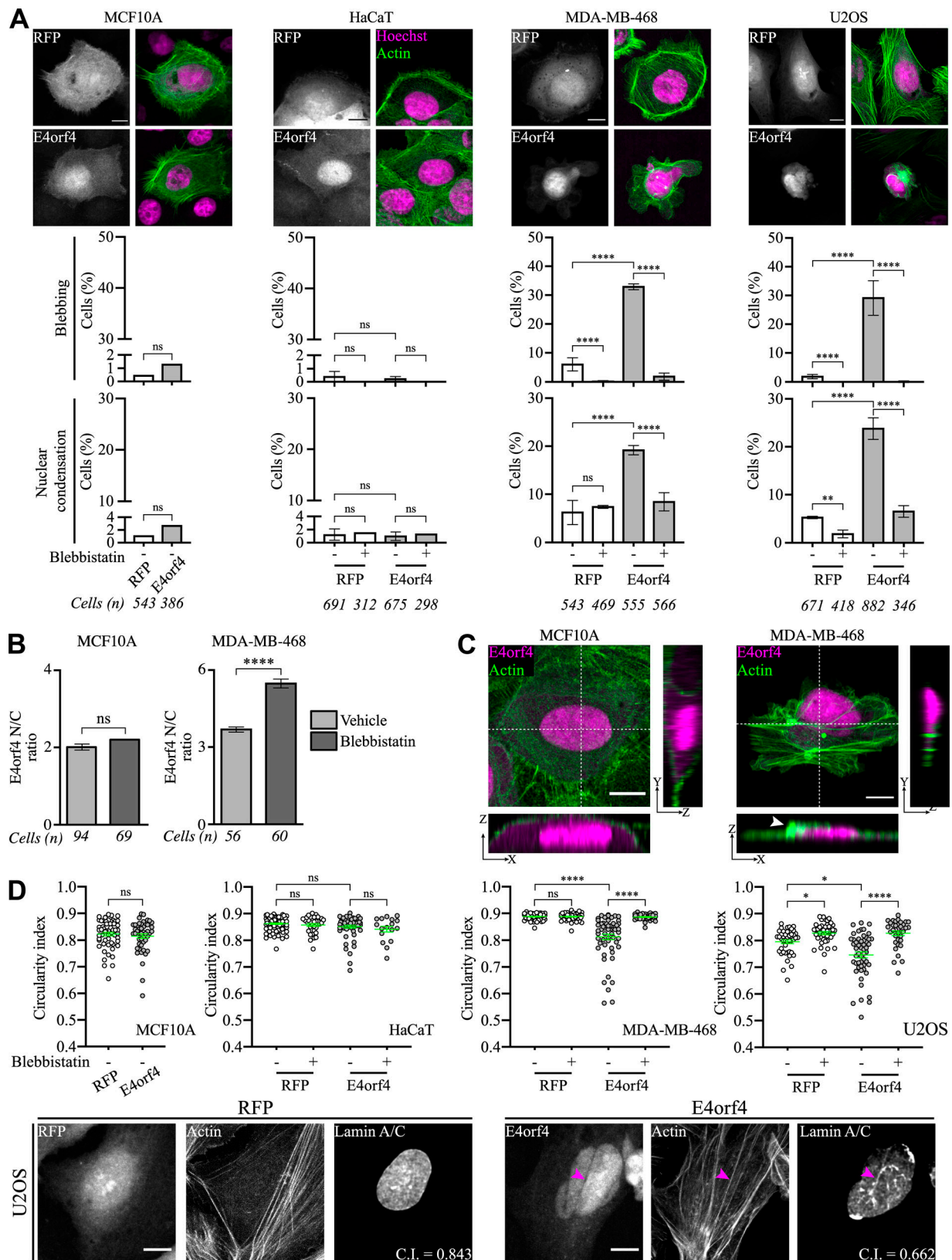


Figure 2. **The tumor cell-selective toxicity of E4orf4 maps to nuclear shape changes regulated by actomyosin contractility.** (A) Deconvolved maximum intensity projections of confocal image stacks of representative RFP- or E4orf4-mCherry-expressing cells showing tumor cell-selective morphological phenotypes associated with cell death (e.g., cell blebbing, F-actin staining in green; nuclear condensation, Hoechst staining in magenta). Bars: 10 μ m. The percentage of cell blebbing and nuclear condensation was scored relative to cells expressing RFP/E4orf4-mCherry 24–36 h after transduction, before and after blebbistatin treatment (50 μ M, 2 h; means [$n > 300$ cells; $n = 2$] or means \pm SEM [$n > 350$ cells; $n \geq 3$]). See also Fig. S1, B and C. (B) Quantification of the

nucleus/cytoplasmic ratio of E4orf4-mCherry, before or after treatment with blebbistatin 2 h (MCF10A: 75 μ M; MDA-MB-468: 50 μ M; means [$n = 2$] or means \pm SEM [$n = 3$]). **(C)** Maximum intensity projections of confocal image stacks showing F-actin clusters (green) proximal to the nucleus (magenta) of a MDA-MB-468-E4orf4 cell, as highlighted on the x-z and y-z views (dotted lines). Bars: 20 μ m. **(D)** Quantification of the nuclear circularity index (C.I.) for datasets acquired as in A (means \pm SEM [$n = 47, 17, 53,$ and 36 cells, respectively, from $n = 3, 2, 3,$ and 3 experiments, respectively]). Maximum intensity projections of RFP- or E4orf4-expressing U2OS cells, showing an early decrease of the nuclear circularity index that matches the presence of lamina folds (lamin A/C staining; magenta arrows) and apical actin filaments at sites where E4orf4 signal is segregated. Bars: 10 μ m. *, $P < 0.05$; ****, $P < 0.0001$; ns, not significant.

recapitulating the effect seen during myosin II inhibition (Fig. 4 E). This result suggests that E4orf4 that is unable to interact with Par3 is retained in the cell nucleus, as it is during the inhibition of cell contractility with blebbistatin.

We next compared the ability of E4orf4 (GGG) to trigger the actomyosin-regulated phenotypes that match E4orf4's tumoricidal activity using U2OS and HeLa cells. These cells display a large projection area and clearly delineated nuclear/cytoplasmic (N/C) boundaries that facilitate quantification of morphological changes. Remarkably, E4orf4 (GGG) showed a severe loss of function, being unable to efficiently induce cell blebbing and nuclear condensation (Figs. 4 F and S3 C). Importantly, cancer cells expressing E4orf4 (GGG) maintained a relatively circular nucleus with few lamina folds, contrary to cells expressing E4orf4 (WT) showing a reduction of nuclear circularity (Figs. 4 G and S3 C). To further interrogate the role of Par3, the phenotypes of E4orf4-expressing cells were analyzed after Par3 depletion using siRNAs or lentivirus carrying Par3-specific shRNAs. We found that Par3 depletion blocked E4orf4-induced cell blebbing and nuclear condensation by >50% in both U2OS and HeLa cells (Fig. 5, A and B). Furthermore, Par3 depletion also prevented E4orf4-induced nuclear deformations and lamina folds, as observed with blebbistatin treatment (Fig. 5 C; and Fig. S4, A and B). The tumoricidal phenotypes, which were also impaired in 293T-shPar3 cells, were restored by the reintroduction of rat GFP-Par3, corroborating a Par3-specific effect. As expected, Par3-GFP constructs with functional domain deletions were unable to restore the tumoricidal phenotypes (Fig. S2, F-J). These results support the requirement of Par3 for a scaffolding-related function.

Since similar phenotypes could be achieved by either depleting Par3 or inhibiting myosin II, we analyzed the impact of Par3 on E4orf4-induced actomyosin contractility. Immunoblotting of myosin light chain phosphorylation (Thr18/Ser19) revealed that E4orf4-induced myosin II activation was not significantly inhibited by Par3 depletion (Fig. 5 D, PP-MLC2; Robert et al., 2006). This result indicates that Par3 may act in parallel to promote actin structure reorganization.

Par3 engages an E4orf4 positive feedback loop, which causes E4orf4's nuclear exit by nuclear bleb rupture

To determine how Par3 and actomyosin contractility regulate E4orf4 spatial dynamics leading to tumoricidal phenotypes, the reversible action of blebbistatin on E4orf4 spatial dynamics was harnessed. This permitted the synchronization of cells expressing mainly nuclear E4orf4 while blocking nuclear shape changes (Fig. 6 A, schematics). Blebbistatin removal caused the nuclear-to-cytoplasmic ratio of E4orf4 to be restored within 1 h (Fig. 6 B, blebbistatin + 60' release). The associated changes to

nuclear shape were imaged by real-time spinning disk confocal microscopy.

Live-cell imaging revealed that cancer cells from diverse origins expressing E4orf4 commonly showed a high frequency of nuclear blebs (Fig. 6 C, blebbistatin + 30' release; Fig. 6 D, control siRNA [siCTL]; and Fig. 6, G and H). Single cells often have at least three voluminous blebs during a 3-h imaging period and more than eight blebs during a 12 h-period (HeLa cells and U2OS and MDA-MB-468 cells, respectively; Fig. 6, D, E, and H). Several nuclear blebs collapsed in the cytoplasm, provoking a sudden nuclear efflux of E4orf4 (Fig. 6, D and G, see "Rupture" on heatmap-colored images; Video 1, E4orf4+siCTL compared to Video 2, RFP only; and Videos 3 and 4, arrows). In contrast, cells expressing a nuclear-targeted RFP or GFP protein only showed a much lower frequency of nuclear bleb formation, which was not associated with the nuclear marker efflux (Fig. 6 H and Video 2). E4orf4-induced nuclear bleb formation was also observed at a high frequency in cells that were not treated with blebbistatin, ruling out a drug-sensitizing effect (~46.8%; Fig. 6 C, vehicle). Importantly, recurrent nuclear bleb formation was markedly decreased by depletion of Par3 (~38% to 68% inhibition; Fig. 6 E, siPar3-3 and 3-9; and Fig. 6 I, shPar3B), while the proportion of nuclear blebs that resorbed was increased (~37.5% in siPar3 versus ~15.5% in siCTL; Fig. 6, D and F; and Video 1, E4orf4+siPar3). Such effects are consistent with a reduction of cytoplasmic E4orf4 upon Par3 depletion and suggest that E4orf4 exits the nucleus through nuclear bleb ruptures (Fig. 5 E).

Nuclear bleb collapse could reflect transient NE ruptures due to focal forces generated by perinuclear actin structures (Hatch and Hetzer, 2016; Le Berre et al., 2012; Robijns et al., 2016; Vargas et al., 2012). Recent findings revealed that cancer cells are prone to undergo transient NE rupture and repair when they are submitted to physical constraints, a feature that could sensitize them to E4orf4 action (De Vos et al., 2011; Denais et al., 2016; Foster et al., 2010; Lammerding et al., 2004; Raab et al., 2016; Vargas et al., 2012). To directly determine nuclear integrity, E4orf4-mCherry was coexpressed with a GFP protein fused to an NLS. The GFP-NLS reporter exhibits rapid efflux bursts into the cytoplasm upon NE rupture and is then gradually reimported into the nucleus as NE integrity is restored. Control cells in interphase displayed a low incidence of NE rupture/repair (HeLa cells: ~10% over a 10 h-period, Fig. 7 B; U2OS cells: ~4.8% over a period of 4 h, Fig. 7 E). In contrast, ~44.5% to 61.3% of E4orf4-expressing U2OS and HeLa cells, respectively, showed NE ruptures associated with a sharp drop of GFP-NLS nuclear intensity as it spilled into the cytoplasm (Fig. 7, A-C and E; and Videos 5 and 6, rupture and repair). Strikingly, repetitive cycles of NE rupture/repair were associated with a loss of NE integrity in ~15% to 25% of E4orf4-expressing cells (Fig. 7, B and C, asterisk;

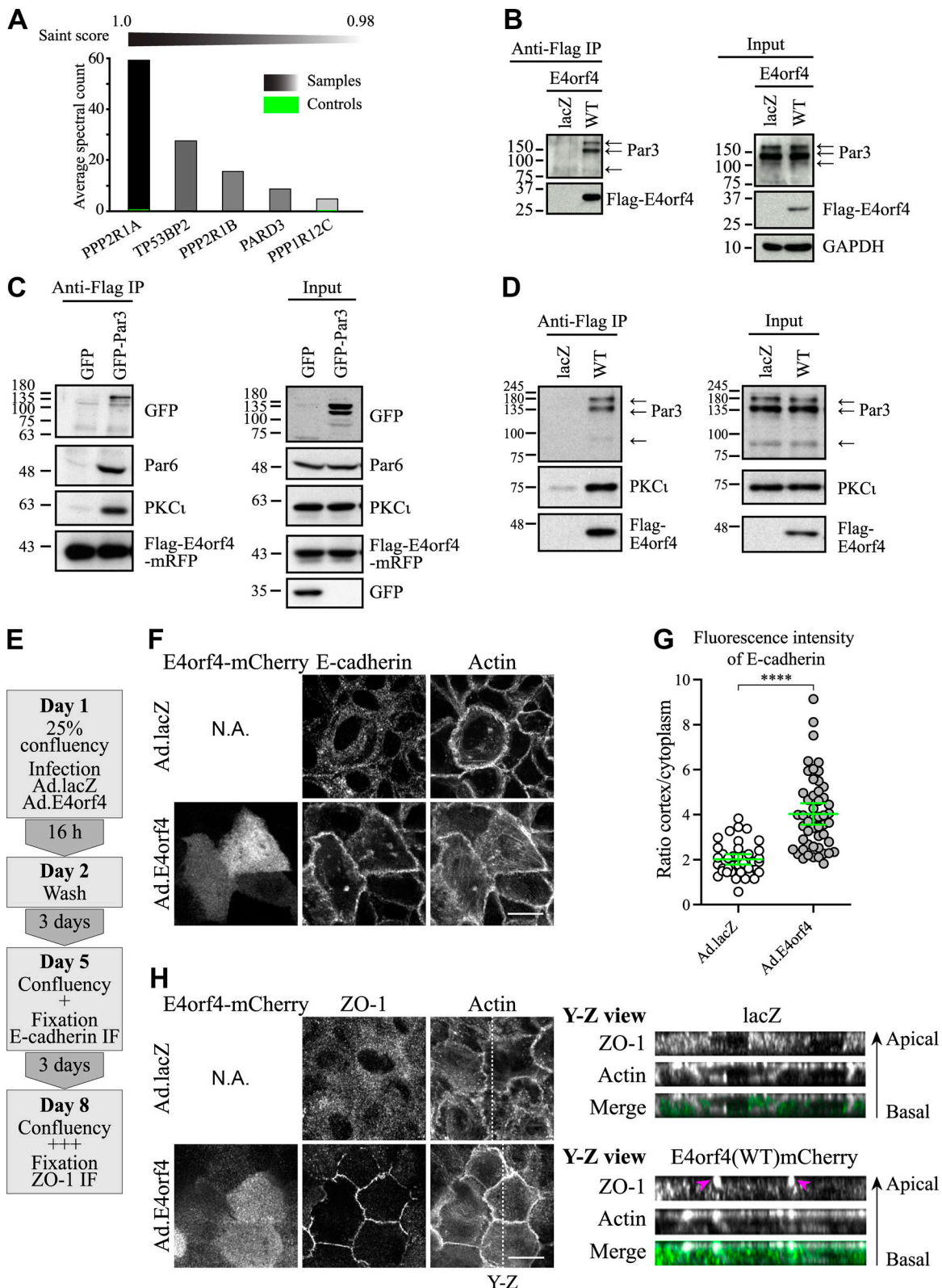


Figure 3. **E4orf4 interacts with Par3 and modulates cell polarity signaling.** (A) Flag-AP-MS identification of Flag-E4orf4's partner proteins, as analyzed by the SAINT algorithm. High-confidence interactors were ranked according to their score (graph), and the average spectral count in the control (green) or E4orf4 sample (gray) is shown; three independent experiments are quantified on the y axis. (B) Flag-E4orf4 IP prepared from MDA-MB-231 cells expressing Flag-E4orf4 followed by IB for Par3 isoforms (arrows); the levels of Flag-E4orf4 in total cell extracts (Input) and GAPDH as loading control are shown (representative of $n = 3$). (C and D) Flag-E4orf4 IPs from 293T-shPar3#4 cells transfected with GFP or GFP-Par3 and Flag-E4orf4-mRFP or from MCF10A cells transduced with lacZ or E4orf4-mCherry (D), followed by IB with the indicated antibodies; Input: total cell extracts; arrows: Par3 isoforms; $n = 2$. (E) Schematic of the protocol

used. **(F and H)** Merged plane views from confocal image stacks of MCF10A cells transduced with lacZ or E4orf4 showing staining of E-cadherin or ZO-1; F-actin was labeled with phalloidin; N.A., not applicable. The dotted lines in H indicate the position of the y axis presented as y-z views on the right panels; magenta arrowheads indicate ZO-1 clusters induced by E4orf4 ($n \geq 3$). Bars: 20 μm . **(G)** Quantification of the cortical/cytoplasmic ratio of E-cadherin for datasets represented in F; means \pm 95% CI; ****, $P < 0.0001$.

Fig. 7 E; and Video 6, bottom cell). In cells depleted of Par3, nuclear ruptures and loss of NE integrity were reduced by $\sim 50\%$ and $\sim 73\%$, respectively (Fig. 7 E).

E4orf4-induced NE rupture is potentially regulated by nucleocytoskeletal connections, such as NE rupture caused by contractile actin bundles (Hatch and Hetzer, 2016). To evaluate this possibility, cells were transduced with lentiviruses carrying shRNA sequences to deplete SUN1/2 proteins and disrupt the LINC complex that connects perinuclear actin bundles to the NE. SUN1/2 proteins were efficiently depleted in U2OS cells using a mixture of two distinct shRNA sequences for each protein, as reported previously (Fig. 7 D; Guilluy et al., 2014). When E4orf4-mRFP and the GFP-NLS reporter were imaged in these cells, a significant reduction in nuclear blebs and NE ruptures were observed (Figs. 6 I and 7 E; $\sim 75\%$ – 85% inhibition). Under these conditions, E4orf4-induced nuclear dysmorphia was not significantly present as compared with RFP-expressing cells (Fig. 7 F; circularity index). Furthermore, E4orf4-induced cell blebbing and nuclear condensation were dramatically impaired (inhibited by $\sim 55\%$ to 67% ; Figs. 7 G and S4 C). Transfection of a dominant-negative GFP-KASH2 to disrupt the binding of endogenous nesprins to SUN proteins also interfered with E4orf4 phenotypes in HeLa cells ($\sim 27\%$ inhibition; Fig. S5, A–C; Stewart-Hutchinson et al., 2008). These results strongly suggest that E4orf4's tumoricidal effect is linked to a subversion of nucleocytoskeletal coupling. Moreover, they argue that a positive feedback loop ascribed to NE rupture and nuclear E4orf4 efflux would exacerbate the actomyosin forces transmitted to the nucleus and jeopardize nuclear integrity.

Localization of Par3 proximal to nuclear lamina grooves is associated with a directional movement of actin filaments and NE rupture

Results suggest that Par3 could function to link actomyosin contractility and nuclear shape changes in response to E4orf4. In line with these findings, Par3-GFP was recruited to perinuclear actin structures that are associated with nuclear dysmorphia (Fig. S5 D). Since exogenous Par3-GFP tended to spontaneously cluster (Fig. S5 D), we immunostained fixed cells for endogenous Par3 in order to examine the impact of E4orf4 by high-resolution confocal imaging. The signal specificity was confirmed in cells transfected with Par3-specific siRNAs (Fig. S5 E). Airyscan confocal imaging revealed that E4orf4 modulated the localization of Par3 in tumorigenic U2OS cells but had little effect in HaCaT, a nontumorigenic cell line expressing similar Par3 levels (The Human Protein Atlas). In U2OS cells, E4orf4 induced Par3 clustering that segregated around the nucleus, contrasting with a relatively diffuse localization of Par3 in unpolarized, exponentially growing HaCaT cells (Fig. 8, A and B; Facciuto et al., 2014). The distinct localization of Par3 was clear upon quantification of Par3–lamin A/C dual-labeled fixed cells on single-slice high-resolution confocal images, highlighting an overlap between

NE and Par3 only in E4orf4-expressing U2OS cells (Fig. 8 C). Most remarkably, Par3 clusters showed a clear alignment with NE folds at the nuclear surface, suggesting that Par3 may delineate sites of nuclear mechanical compression (Fig. 8, D and E).

To directly investigate the relationships among Par3, actin structure dynamics, and nuclear shape changes, U2OS cells co-expressing E4orf4-mCherry and LifeAct-GFP were imaged to track the behavior of actin structures within cells in relation to NE rupture (Videos 7, 8, and 9). In E4orf4-cells transfected with siCTL, actin structures mainly exhibited a directional movement toward and over the nucleus, which coincided with nuclear bleb formation and nuclear E4orf4 efflux due to NE rupture (Fig. 9 A, siCTL arrows; and Videos 7 and 9). This directional and retrograde movement of actin structures was disrupted by Par3 depletion, as evidenced by kymograph measurements (Fig. 9 A, siPar3, dotted line; Fig. 9, B and C; and Video 8). Quantification of actin structure velocity revealed that in control E4orf4-cells, actin filaments moved toward the nucleus with an average speed of $0.129 \mu\text{m min}^{-1}$ (shown by the peak of the curve), while in Par3-depleted cells, they barely moved toward the nucleus, with a fivefold reduction in average speed ($0.026 \mu\text{m min}^{-1}$; Fig. 9 C). Importantly, we found a linear correlation between mean average velocity values of actin filaments in single cells and their respective time to nucleus rupture ($R^2 = 0.8945$; Fig. 9 D). Notably, among the Par3-depleted cells, the few that showed NE rupture also displayed higher actin filament velocities and positive movement values toward the nucleus (white circles, Fig. 9 D). Together, the results suggest that Par3 clustering at the NE can direct a retrograde movement of actin structures that contributes to increasing nuclear mechanical stress.

Par3 regulates spontaneous NE rupture facilitated by downmodulation of lamins

Finally, the impact of Par3 on NE rupture mediated by actin-based nucleus confinement in the absence of E4orf4 was determined. To this end, lamina proteins were partially depleted to recapitulate lamina deficiencies and induce spontaneous NE rupture, as reported before (Hatch et al., 2013; Hatch and Hetzer, 2016). HeLa cells were transfected with a mixture of lamin A/C- and lamin B1-specific siRNAs that achieved moderate lamin depletion and increased the occurrence of spontaneous NE rupture by approximately twofold as assessed by live-cell imaging of the RFP-NLS marker (Fig. 10, A–C; and Video 10; Vargas et al., 2012). Strikingly, when Par3 was also depleted in these cells, the occurrence of spontaneous NE ruptures was reduced back to near the basal levels observed in control cells (siCTL), even though lamins were similarly depleted (Fig. 10, B and C). These results suggest that depletion of Par3 alleviates the actin-dependent constraints on the nucleus that cause NE rupture. We conclude that Par3 is a bona fide regulator of the actin-dependent forces controlling nuclear mechanics in tumor cells.

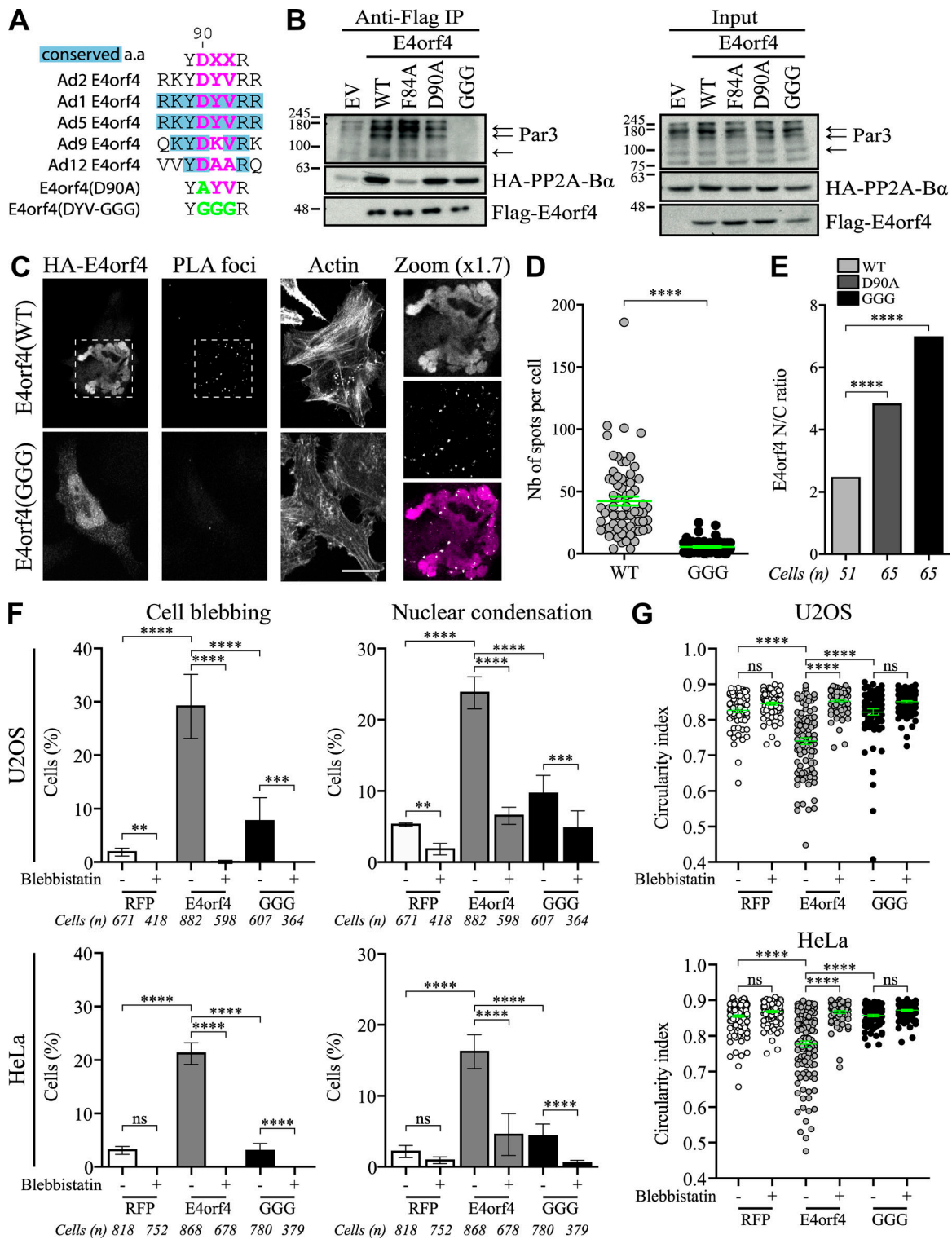


Figure 4. Binding to Par3 regulates E4orf4 toxicity in cancer cells. (A) Sequence alignments of the Par3-binding motif on E4orf4 in type 2 Ad and other serotypes (in magenta); conserved residues are highlighted in blue, and residue substitutions to generate the E4orf4 mutants are indicated in green. EV, empty vector. (B) Flag-E4orf4 IPs prepared from 293T cells transfected with Flag-E4orf4 constructs and HA-PP2A-B α , followed by IB with the indicated antibodies; Input: total cell extracts; arrows: Par3 isoforms; $n = 3$. (C) Merged plane views from confocal image stacks of representative HeLa cells expressing E4orf4 (WT or GGG), showing PLA signal and HA-E4orf4 staining detected with anti-mouse-Alexa antibody; actin was stained using phalloidin. Bar: 20 μ m. (D) Quantification of the number of PLA foci per cell; means \pm SEM ($n \geq 58$ cells; $n = 3$). (E) Quantification of the N/C ratio of E4orf4-mCherry for datasets represented in Fig. S3 C; means ($n \geq 51$ cells; $n = 2$). (F) The percentage of cell blebbing and nuclear condensation was scored relative to U2OS or HeLa cells expressing RFP or E4orf4 (WT or GGG; means \pm SEM [$n \geq 3$]). (G) Quantification of the nuclear circularity index of cells fixed at 24–36 h after transduction, before and after blebbistatin treatment (50 μ M, 2 h), for the datasets represented in Fig. S3 C (means \pm SEM [$n \geq 67$ cells; $n = 3$]). **, $P < 0.01$; ***, $P < 0.001$; ****, $P < 0.0001$; ns, not significant. See also Figs. S2 and S3 C.

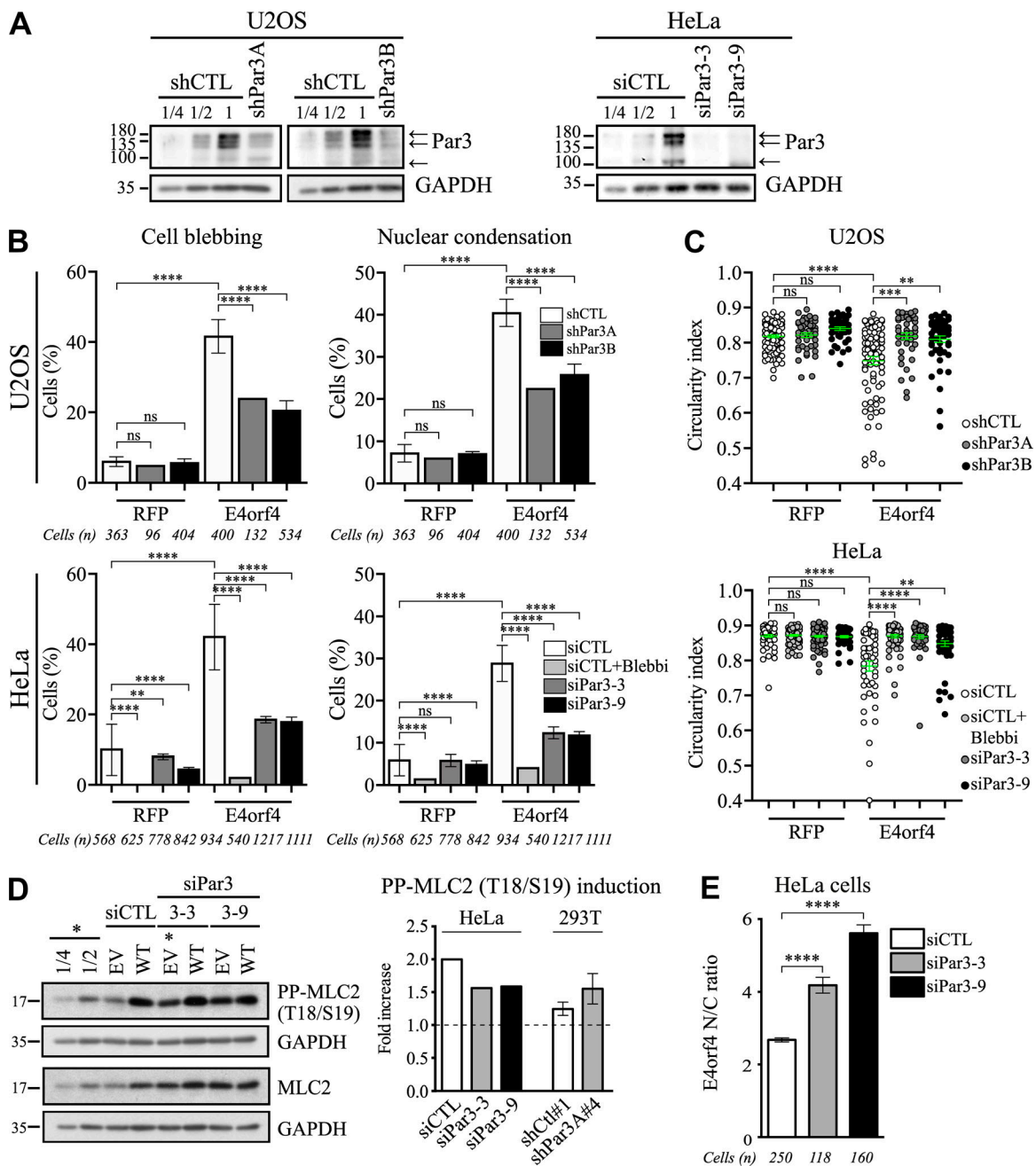


Figure 5. **Par3 depletion inhibits E4orf4 tumoricidal phenotypes.** (A) Representative IBs of Par3 depletion in U2OS cells (shPar3A and B) and HeLa cells (siPar3-3 and 3-9), as estimated by loading increasing amounts of control extracts (shCTL or siCTL, 1, 1/2, and 1/4); GAPDH, loading control. (B) The percentage of cell blebbing and nuclear condensation, as scored relative to RFP- or E4orf4-mCherry-expressing cells at 24–36 h after transduction; data from one representative experiment (shPar3A) or means \pm SEM ($n = 3$). (C) Quantification of the nuclear circularity index of cells treated as in B (means \pm SEM [$n \geq 43$ cells; $n \geq 3$]). (D) Representative IBs of extracts from HeLa cells treated with siRNAs and then transfected with the vector (EV) or E4orf4-mRFP (WT); activated myosin II, phospho-MLC2 (T18 and S19); total myosin II, MLC2; GAPDH, loading control. Quantification represents means ($n = 2$; HeLa cells) or means \pm SEM ($n = 4$; 293T-shPar3#4 cells). (E) Quantification of the N/C ratio of E4orf4-mCherry in HeLa cells transfected with siCTL or siPar3 for datasets represented in Fig. S4 B (means \pm SEM [$n \geq 118$ cells; $n = 3$]). **, $P < 0.01$; ***, $P < 0.001$; ****, $P < 0.0001$; ns, not significant. See also Fig. S4 B.

Discussion

Taken together, our data suggest that E4orf4's tumoricidal action involves an early loss of nuclear integrity. This loss is predominantly due to corruption of a new Par3 scaffolding function at the NE, which may control the spatial dynamics of actin structures and thereby force transmission to the nucleus. As a result

of the E4orf4-Par3 interaction, clustering of Par3 could provide spatial information to polarize actin structures and promote their retrograde translocation toward the nucleus, the efficiency of which would depend on nucleocytoskeletal connections (Fig. 10, D and E). We suggest that Par3 enables E4orf4 to engage a positive feedback loop that exploits nucleocytoskeletal coupling

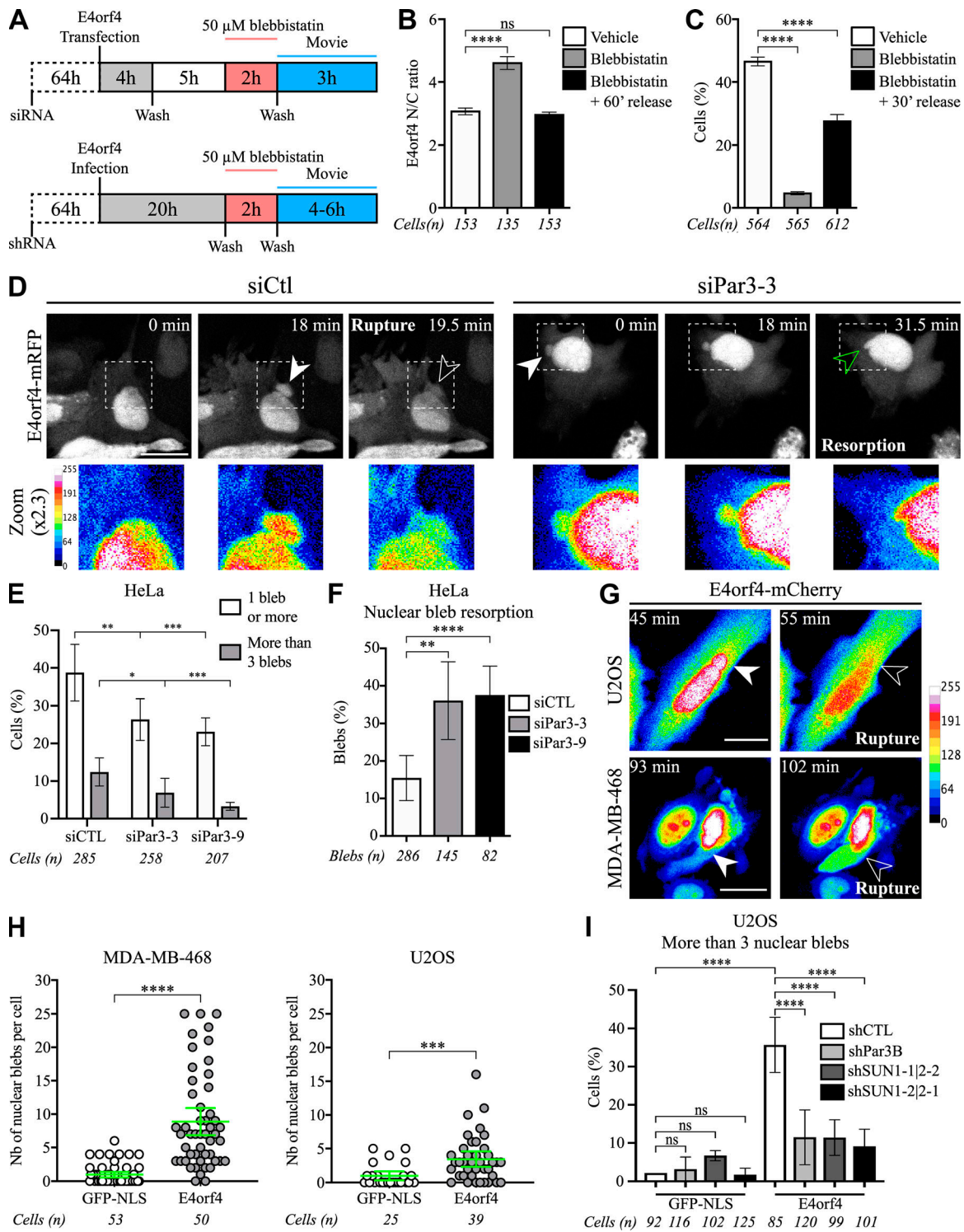


Figure 6. E4orf4 nuclear exit by nuclear bleb formation is inhibited by depletion of Par3 or SUN1/2. (A) Schematics of the protocols. (B) Quantification of the N/C ratio of E4orf4-mRFP in HeLa cells treated with blebbistatin 50 μ M for 2 h and released for 1 h (means \pm SEM [$n \geq 135$ cells; $n \geq 3$]). (C) The percentage of HeLa cells undergoing nuclear bleb (NB) formation (means \pm SEM [$n = 3$]). (D) Video stills taken from live-cell imaging of siRNA-treated HeLa cells transfected with E4orf4-mRFP; filled arrowheads, NB formation; empty arrowheads, NB rupture in siCTL-cells (white, empty), as emphasized by a heatmap applied on the enlarged views, or NB resorption in siPar3-cells (green-empty). Bar: 20 μ m. See also [Video 1](#). (E and F) The percentage of HeLa cells showing at least 1 NB or more than 3 NB, and the percentage of resorbing NB over a 3 h-period, as scored relative to E4orf4-mRFP-expressing cells; means \pm SEM ($n \geq 207$ cells, ≥ 82 blebs; $n \geq 3$). (G and H) Video stills taken from live-cell imaging of E4orf4-mCherry-expressing MDA-MB-468 and U2OS cells; filled arrowheads, NB formation; empty arrowheads, NB rupture and E4orf4 nuclear exit as emphasized by applying a heatmap pseudo-color intensity scale. Bar: 20 μ m. (H) The number of NBs per cell from one representative live-cell imaging of 12 h (MDA-MB-468 cells) or 4 h (U2OS cells; means \pm 95% CI [$n \geq 25$ cells]). See also [Videos 3](#) and [4](#). (I) The percentage of shRNA-treated U2OS cells expressing GFP-NLS or E4orf4-mRFP that showed more than three NBs (means \pm SEM [$n \geq 92$ cells; $n = 3$]). *, $P < 0.05$; **, $P < 0.01$; ***, $P < 0.001$; ****, $P < 0.0001$; ns, not significant.

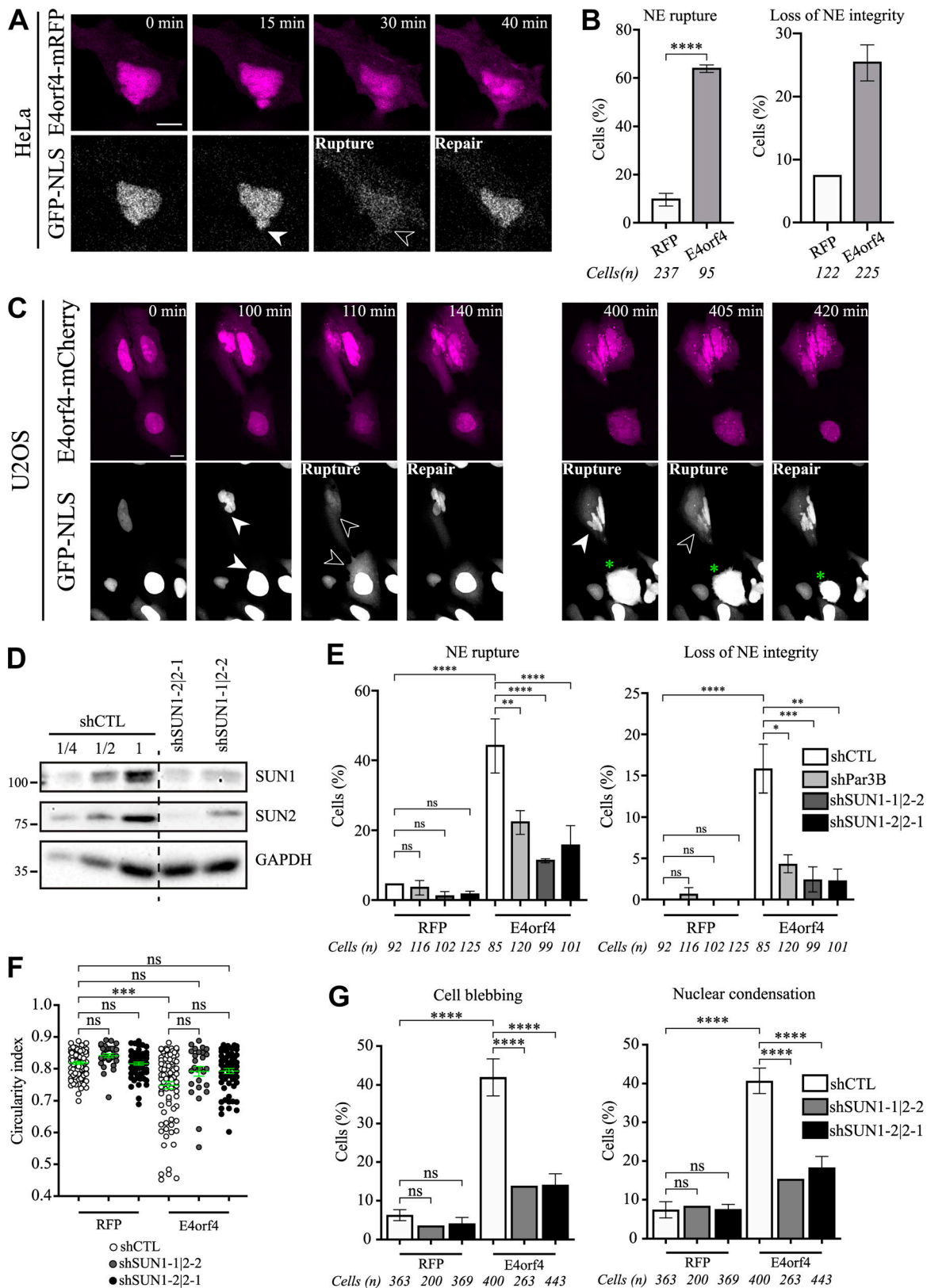


Figure 7. **E4orf4-induced NE rupture is regulated by Par3 and SUN1/2.** (A and C) Video stills taken from live-cell imaging of a representative HeLa cell (A) or U2OS cells (C) expressing E4orf4-mCherry and GFP-NLS. NB growing and transient NE rupture associated with cytoplasmic GFP-NLS signal are designated by filled and empty arrowheads, respectively; the green asterisks in C point to a cell displaying a prolonged loss of nuclear integrity associated with sustained E4orf4 cytoplasmic signal and cell blebbing. Bars: 10 μ m. See also Videos 5 and 6. (B) The percentage of HeLa cells showing transient NE rupture or loss of NE integrity (no repair over >30 min), as scored relative to GFP-NLS-expressing cells (means \pm SEM [$n \geq 95$ cells; $n = 4$]). (D) Representative IB showing SUN1/2

depletion in U2OS cells using mixtures of two sequences targeting SUN1 or SUN2 (shSUN), as estimated by loading increasing amounts of control cell extracts (shCTL or siCTL, 1, 1/2, and 1/4); GAPDH levels, loading control. **(E)** The percentage of shRNA-treated U2OS cells expressing RFP or E4orf4-mCherry together with GFP-NLS as a marker of NE rupture, which showed transient NE rupture or loss of NE integrity (no repair over >30 min), as scored relative to GFP-NLS-expressing cells; data represent means ($n \geq 92$ cells; $n = 2$) or means \pm SEM ($n \geq 85$ cells; $n = 3$). **(F)** Quantification of the nuclear circularity index for datasets represented in Fig. S4 C (means \pm SEM [$n \geq 27$ cells; $n = 4, 2, 4, 4, 2$, and 4 , respectively]). **(G)** The percentage of U2OS cells showing cell blebbing and nuclear condensation, as scored relative to RFP- or E4orf4-mCherry-expressing cells for datasets represented in Fig. S4, B and C (means [$n \geq 200$ cells, $n = 2$] or means \pm SEM [$n \geq 363$ cells; $n = 3$]). *, $P < 0.05$; **, $P < 0.01$; ***, $P < 0.001$; ****, $P < 0.0001$; ns, not significant.

in tumorigenic cells. These cells are more prone to nuclear ruptures, due to their reduced nuclear stiffness and increased actomyosin contractility (Denais et al., 2016; Vargas et al., 2012). This vicious cycle would build upon NE ruptures causing an efflux of E4orf4 and other molecules that would further amplify actomyosin contractility and NE ruptures, ultimately overcoming the cellular capacity to repair the NE. Prolonged NE integrity loss during interphase would perturb several essential functions and jeopardize genomic integrity (Isermann and Lammerding, 2017). We propose that disruption of NE mechanical regulation represents a prime lesion responsible for the extreme alterations of tumor cell structural organization (Lavoie et al., 2010).

We found that disrupting myosin II, Par3, or LINC complex functions can recapitulate the same inhibitory phenotypes on E4orf4-induced morphodynamic changes, suggesting that they act on the same pathway for efficient force transmission to the nucleus. Since Par3 also regulated spontaneous NE rupture induced by lamin depletion, we infer here that a Par3 scaffolding is widely implicated. The exact mechanism whereby Par3 would control the spatial linkage of contractile actin filaments at the nuclear surface is an outstanding issue with potential implications for tumor cell metastatic potential. Metastasizing cancer cells that encounter tight interstitial spaces are particularly prone to transient NE rupture. This process is viewed as a new mechanism dependent on confinement that promotes genomic instability and tumor progression (Calero-Cuenca et al., 2018; Shah et al., 2017). Therefore, such a mechanism could be an important part of the tumor-promoting functions of Par3.

In conclusion, our data indicate that oncogenic rewiring of the Par complex protein network could define novel protein partners for Par3 that regulate NE dynamics, genome integrity, and metastatic potential. In that context, E4orf4 offers a unique tool to uncover new vulnerabilities in malignant cells.

Materials and methods

Expression vectors, mutagenesis, Ads, and baculoviruses

The following expression vectors were described previously: Flag-E4orf4(WT)-mRFP, Flag-E4orf4(F84A)-mRFP, HA-E4orf4(WT) (Champagne et al., 2004; Robert et al., 2006); pEGFP-KASH2 and pEGFP-KASH2ext (Stewart-Hutchinson et al., 2008); and GFP-Par3 (rat Par3 cDNA in pEGFP-C1; Hidalgo-Carcedo et al., 2011). The GFP-Par3 deletion mutants were designed by PCR using rat GFP-Par3 as a template and the following primers:

Par3_DNterm_fwd: 5'-Phos-ATGAAGCTCGTACAAGTCCCCAA-3';
Par3_DNterm_rev: 5'-GGTGGCGATATCGCTAGCAA-3'; rPar3_delPDZ_fwd: 5'-Phos-AGGCGGATCAGCAGATGTAACGAGTTG-3';
rPar3_delPDZ_rev: 5'-TACCATATCATCGAGGAAAAGTTGGGC-3';

rPar3_delPKC_fwd: 5'-Phos-GAGAAGAGGGACAAGGCAGAGAAGAAAAAG-3'; rPar3_delPKC_rev: 5'-GCGTTCTCTGTCTATCCAACCTCTGTTTCTAT-3'; Par3_DCterm_fwd: 5'-Phos-GTCGACGGTACCGCG-3'; Par3_DCterm_rev: 5'-TGGGTCTCCATTCATTTGTC-3'.

GFP-NLS (NLS from SV40 large T antigen: PKKKRKKV) was described before (Robert et al., 2002). E4orf4-D90A and DYV-GGG mutants were designed by PCR using the QuickChange Site-Directed Mutagenesis kit (Stratagene). Flag-E4orf4(WT)-mRFP in pcDNA₃ or the HA-E4orf4(WT) was used as templates with the following primers:

Orf4-D90A.gen: 5'-GCTTCAGGAAATATGCCTACGTCCGGCGTCCATTTGGC-3'; Orf4-D90A.rev: 5'-GCCAAATGGAACGCCGGACGTAGGCATATTTCTGAAAGC-3'; Orf4-DYV-90-91-92-GGG.gen: 5'-GCTTCAGGAAATATGGCGCGCGCGGCGTTCATTTGGC-3'; Orf4-DYV-90-91-92-GGG.rev: 5'-GCCAAATGGAACGCCGGCGCGCCATATTCTGAAAGC-3'.

All constructs were confirmed using DNA sequencing. Ad-LacZ and Ad-GFP were described previously (Smadja-Lamère et al., 2008). Ad-Flag-E4orf4(WT)-mCherry, Ad-Flag-E4orf4(F84A)-mRFP, and Ad-Flag-E4orf4(GGG)-mRFP were produced by Welgen. Adenovirus type C strain 5 containing the different E4orf4 variants was produced by subcloning into recombinant adenoviral vector lacking the E1 and E3 regions. The E1 deletion was replaced with an expression cassette consisting of a cytomegalovirus promoter with a bacterial tetracycline resistance operon, the gene of interest, and a poly A signal. Recombinant Ads were amplified in the HEK293VR cell line expressing the tetracycline repressor (a gift from Philip E. Branton, McGill University, Montreal, Québec, Canada). All recombinant Ads were confirmed by sequencing of the inserted sequences. Virus titers were determined using the AdenoX Rapid titer kit (Clontech Laboratories; #631028). Baculovirus encoding RFP-NLS or GFP-NLS were purchased from Invitrogen/Thermo Fisher Scientific (CellLight Nucleus-RFP, BacMam 2.0, C10603; CellLight Nucleus-GFP, BacMam 2.0, C10602).

Lentivirus-shSUN1/2 production

The following individual SUN1- and SUN2-specific shRNAs were engineered using two oligonucleotides (IDT) that were annealed, phosphorylated, and ligated into AgeI and EcoRI restriction sites of pLKO.1 vector (Addgene; plasmid #8453): shSUN1-1 (5'-CCG GCAGATACACTGCATCATCTTTCTCGAGAAAGATGATGCAGTG TATCTGTTTTTTG-3' and 5'-AATTCAAAAAACAGATACACT GCATCATCTTTCTCGAGAAAGATGATGCAGTGTATCTG-3'), shSUN1-2 (5'-CCGGAACTAGAACAGACCAAGCAACTCGAG TTGCTTGGTCTGTTCTAGTTCTTTTTTTG-3' and 5'-AATTCA AAAAAGAACTAGAACAGACCAAGCAACTCGAGTTGCTTG GTCTGTTCTAGTTC-3'), shSUN2-1 (5'-CCGGGCTATTTCAGACGTT TCACTTCTCGAGAAGTGAACGCTCTGAATAGGCTTTTTTTG-3' and

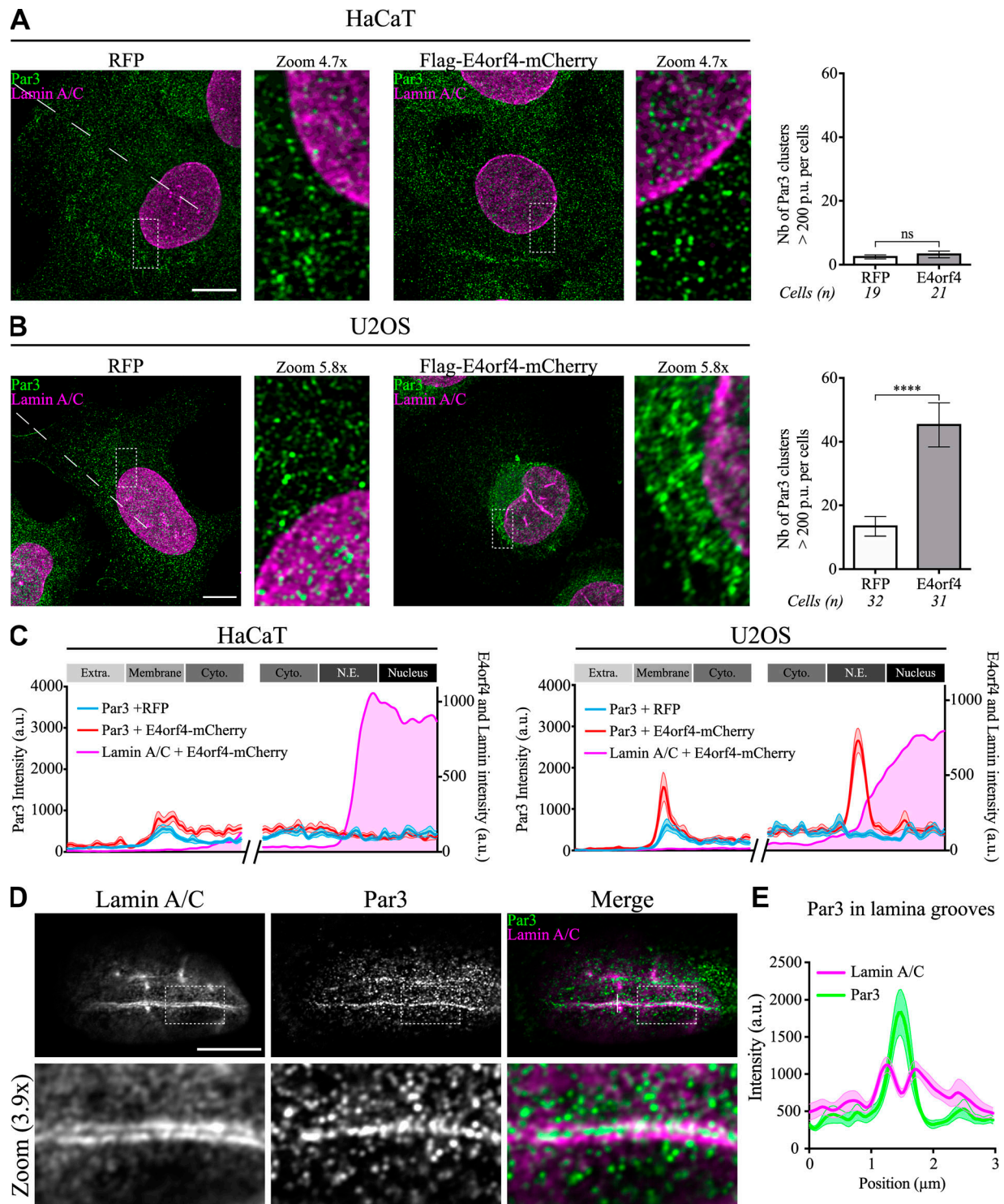


Figure 8. **E4orf4 recruits Par3 to the nuclear lamina in tumorigenic cells.** (A and B) Representative single-plane Airyscan confocal images of HaCaT (nontumorigenic) and U2OS cells (tumorigenic) showing endogenous Par3 (in green) and lamin A/C staining (in magenta). Graphs show the number of Par3 clusters per cell with a relative area ≥ 200 pixel units (p.u.); data represent means \pm SEM ($n = 19, 21, 32,$ and 31 cells, respectively). (C) Quantification of Par3 intensity profiles for the datasets represented in A and B showing the means (solid lines) and SEM (shaded areas; $n = 20, 20, 19,$ and 22 cells), as measured along a $5 \mu\text{m}$ section that spanned the extracytoplasmic to the nuclear regions (dotted lines) by taking two measurements per cell; Cyto, cytoplasmic; Extra, extracellular. The intensity profiles of lamin A/C in E4orf4-expressing cells are shown as a reference. (D) Representative single-slice Airyscan confocal images of a nucleus from an E4orf4-expressing U2OS cell showing Par3 clusters (in green) decorating the center of a lamina groove delineated by lamin A/C staining (in magenta). (E) Quantification of Par3 intensity profiles compared with lamin A/C at lamina grooves for datasets represented in D showing average (solid line) and SEM (shaded area; $n = 14$ cells), as measured along a $3\text{-}\mu\text{m}$ section perpendicular to a lamina groove (dotted line in enlarged view). Bars: $10 \mu\text{m}$. ****, $P < 0.0001$; ns, not significant.

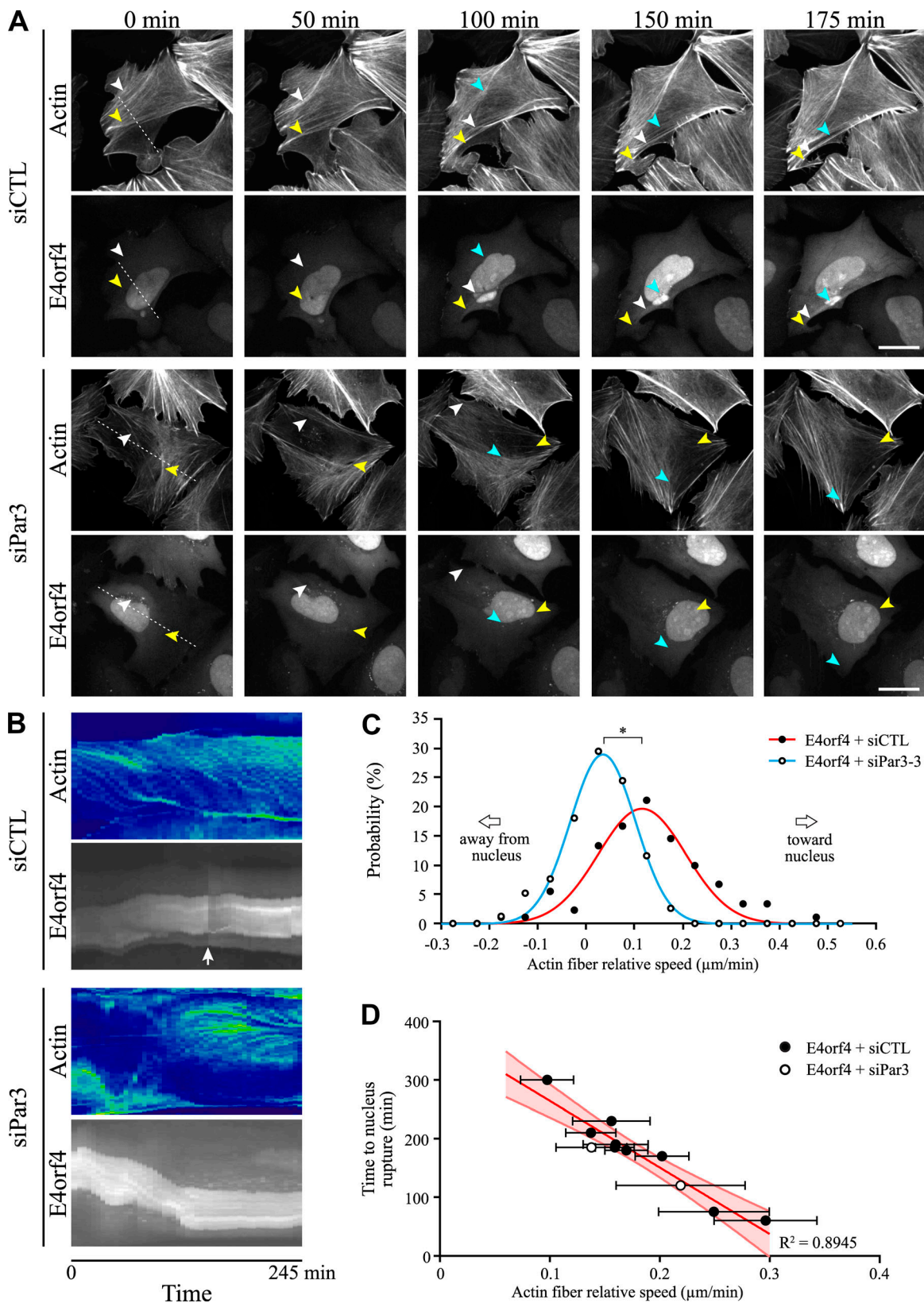


Figure 9. **A** Par3-regulated retrograde movement of actin structures toward the nucleus correlates with NE rupture. **(A)** Video stills taken from 3D-cell imaging of representative U2OS cells treated with siCTL or siPar3, expressing E4orf4-mCherry and the actin marker LifeAct-GFP, showing the movement of actin structures over time relative to E4orf4 nuclear signal, as pointed by colored arrowheads; actin filaments move directionally toward the nucleus in siCTL-treated cells, whereas they move randomly in siPar3-treated cells. Bar: 20 μm . See also Videos 7, 8, and 9. The dashed lines identify the cross sections perpendicular to actin network at $t = 0$ min. **(B)** Corresponding kymographs of actin structure dynamics (in pseudo-color); E4orf4 signal along the cross

sections is shown as a reference (in gray), and the arrow designates the time of NE rupture in a siCTL-treated cell. **(C)** Quantification of actin structure velocity toward the nucleus in E4orf4-expressing cells, as measured from the probability distribution from all the visible actin structure velocity distributions; siCTL, ●, $n = 9$ cells; siPar3, ○, $n = 8$ cells. The plain lines provide the Gaussian fit of the normal distribution. Actin structures moving toward the nucleus were defined as having a positive speed, whereas those moving away as having a negative speed. **(D)** Linear plot of the time of nuclear rupture as a function of the speed of actin structures toward the nucleus, showing a linear relationship ($R^2 = 0.8945$); each data point corresponds to the average actin speed \pm SD and rupture time ± 2.5 min (e.g., half the acquisition rate) for a single cell, and the shaded area provides the 95% CI of the linear regression. *, $P < 0.05$.

5'-AATTCAAAAAAGCCTATTCAGACGTTTCACTTCTCGAGAAGT GAAACGTCTGAATAGGC-3'), shSUN2-2 (5'-CCGGCAAGACTCAG AAGACTCTTCTCGAGAAGAGGTCTTCTGAGTCTTCTTTTTTGG-3' and 5'-AATTCAAAAAAGCAAGACTCAGAAGACTCTTCTCGAGA AGAGGTCTTCTGAGTCTTGC-3'); underlined sequences represent the targeted sequences. For double knockdown of SUN1 and SUN2, pLKO.1 vector containing shSUN2 was amplified by PCR using primers 5'-TTTAAATAGAATTCGAGACTAGCCTCGAGCGGC-3' and 5'-TGCCATTTGTCTCGAGGTGCA-3' in order to produce a sequence with the U6 promoter followed by shRNA. After digestion by EcoRI, this sequence was ligated into EcoRI restriction sites of pLKO.1 vector containing shSUN1 to generate shSUN1-1/2-2 and shSUN1-2/2-1. Lentiviral particles were generated by transfecting 293T cells with 12 μ g pLKO.1 vector, 6 μ g psPAX2 packaging plasmid (Addgene; plasmid #12260), and 2 μ g pMD2.G envelope plasmid (Addgene; plasmid #12259), as described previously (Bergeman et al., 2016).

Antibodies and chemicals

The following antibodies and drugs were used: Anti-Par3 (#07-330) was from Millipore; anti-GFP 3E6 (A11120) for IP was from Molecular Probes; anti-Flag M2 (F3165) and anti-vinculin (V9131) were from Sigma-Aldrich; anti-RFP (600-401-379) was from Rockland; anti-E-cadherin (610181) and anti-PKC α (610175) were from BD Transduction Laboratories; anti-GAPDH ZG003 (39-8600) and anti-ZO-1 1A12 (33-9100) were from Thermo Fisher Scientific; anti-GFP B-2 for Western blot (sc-9996), anti-lamin A/C 636 (sc-7292) for immunofluorescence (IF) anti-myosin light chain 2 (sc-15370), and anti-Pard6B H-64 (sc-67392) were from Santa Cruz; anti-lamin B1 (ab16048) and anti-lamin A/C for Western blot (ab133256) were from Abcam; anti-HA.11 (MMS-101R) was from Covance; and anti-phospho-myosin light chain 2 (Thr18/Ser19; 3674) and anti-phospho(Ser) PKC substrate (2261) were from Cell Signaling Technologies. Blebbistatin (203390) was purchased from Calbiochem; fibronectin (F1141) and puromycin (P8833) were purchased from Sigma-Aldrich; and Alexa-Fluor phalloidin was purchased from Molecular Probes/Thermo Fisher Scientific.

Cell culture and generation of stable cell lines

HeLa CCL-2 cells (American Type Culture Collection [ATCC]) was maintained in α MEM with 10% FBS (Wisent); 22Rv1 cells (a gift from Frédéric Pouliot, Université Laval, Québec City, Québec, Canada; Neveu et al., 2016) were maintained in RPMI-1640 (Gibco) with 10% FBS; MDA-MB-231 cells (ATCC) were maintained in Leibovitz's L-15 or RPMI-1640 with 10% FBS; MDA-MB-468 cells (ATCC) were maintained in Leibovitz's L-15 with 10% FBS; HEK293T, U2OS (a gift from Jacob Nilsson, University of Copenhagen, Copenhagen, Denmark; Sedgwick et al.,

2013), HaCaT (a gift from Jacques Huot, Université Laval; Boukamp et al., 1988), and hTERT RPE-1 cells (ATCC) were cultured in high-glucose DMEM (GIBCO) with 10% FBS; MCF10A cells (ATCC) were cultured in DMEM F12 with 5% horse serum, 0.5 μ g/ml hydrocortisone, 10 μ g/ml insulin, 20 ng/ml epithelial growth factor, and 100 ng/ml cholera toxin (Sigma-Aldrich) and maintained as described previously (Debnath et al., 2003). Cells were grown in a humidified atmosphere in 5% CO₂ or in 0% CO₂ when cultivated in Leibovitz's L-15 medium. MCF10A, HaCaT, hTERT RPE1, 22Rv1, HeLa-CCL2, U2OS, and MDA-MB-231 cell lines were verified using short tandem repeat profiling (ATCC human short tandem repeat profiling cell authentication service). All cell lines were tested negatively for mycoplasma contamination.

293T-shCTL and 293T-shPar3 stable lines were generated using the MISSION shRNA kit (Sigma-Aldrich). 293T cells (ATCC) were transduced with 0.3 colony-forming units of lentivirus, and stable clones were selected with 3 μ g/ml puromycin, isolated, and assayed for their level of Par3 knockdown by Western blot analyses. The MISSION shRNA transduction particles were as follows: shPar3A, reference. TRCN0000118134; sequence, 5'-CCGGCCATCGACAAATCTTATGATCTCGAGATCAT AAGATTTGTGATGGCTTTTTTGG-3'.

Transfection and siRNA experiments

Plasmid transfection was performed using Lipofectamine 2000 or Lipofectamine 3000 (Thermo Fisher Scientific; HeLa and U2OS cells) or the calcium-phosphate method (293T cells; Champagne et al., 2004). For siRNA transfection, cells were plated on 35-mm Petri dishes and cultured for >16 h before transfection. siRNA duplexes were transfected overnight at 50–60 nM using the RNAiMax transfection reagent (Invitrogen). Cells were washed, replated at a 1/7 dilution in 35-mm Petri dishes, and cultured for at least 48 h before performing subsequent analyses. The siRNA duplexes were purchased from Thermo Fisher Scientific (standard A4 grade); sequences of the sense strands are as follows: siPar3-3, 5'-GAU GGCGACCUUCGAAAUUU-3'; siPar3-9, 5'-GGGCAAAUCCCA AGAGGAAUU-3'; siLamin A/C, 5'-UGUUCUUCUGGAAGUCCA GUU-3'; and siLamin B1, 5'-CGCGCUUGGUAGAGGUGGAUU-3' (Vargas et al., 2012). Control siRNA (siCTL): AllStars Negative Control was purchased from Qiagen, target sequence: 5'-CAG GGTATCGACGATTACAAA-3'.

Cell transduction with viral vectors

Adenovirus and baculovirus infections were performed in cell suspension in culture medium supplemented with 8 μ g/ml polybrene (Sigma-Aldrich). HeLa ($2 \times 10^5/2$ ml), U2OS ($1.75 \times 10^5/2$ ml), 22Rv1 ($4 \times 10^5/2$ ml), MDA-MB-231 ($2.75 \times 10^5/2$ ml),

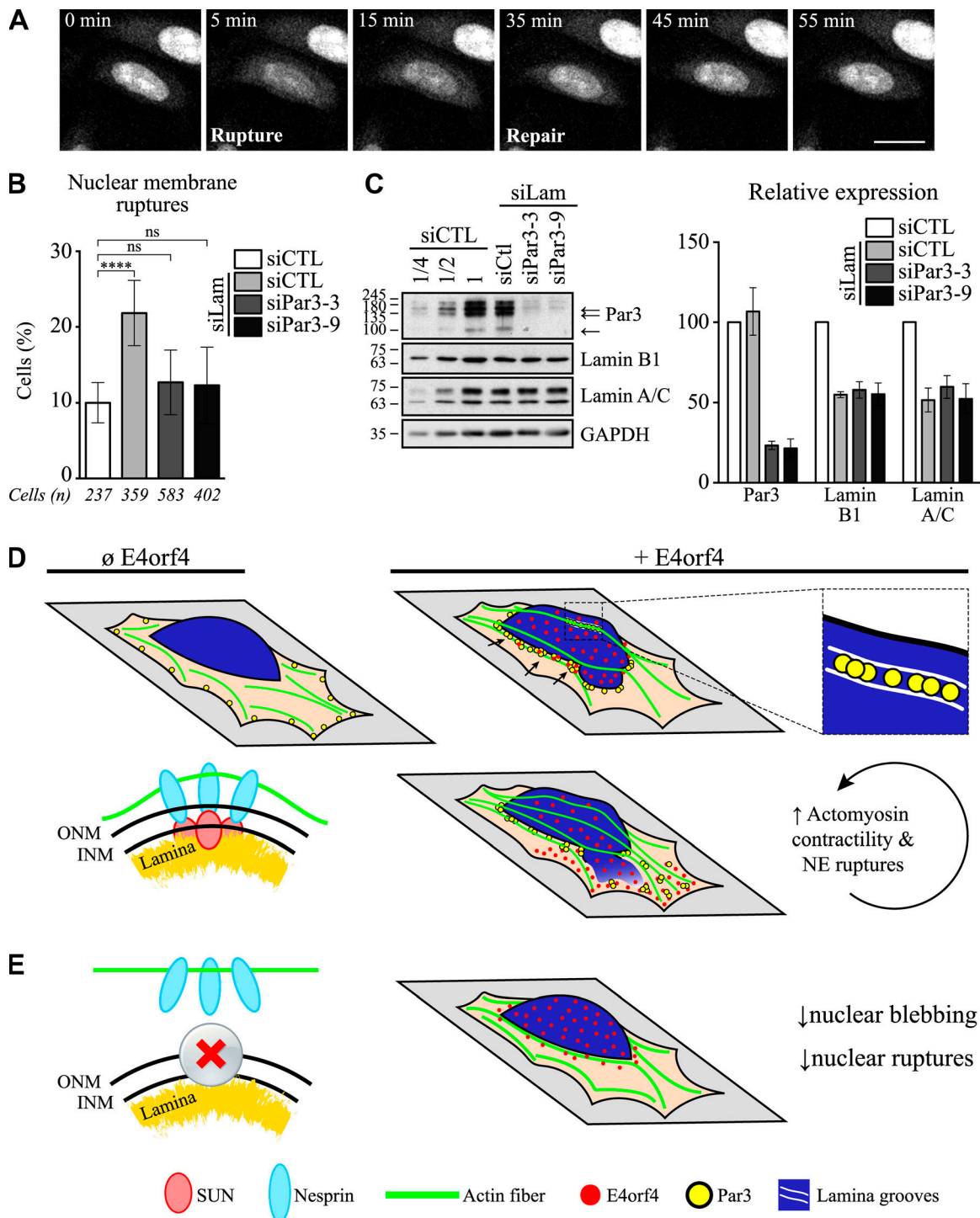


Figure 10. **Par3 regulates the incidence of spontaneous NE ruptures.** (A) Video stills taken from 2D-cell imaging of a representative RFP-expressing HeLa cell transfected with a mixture of lamin A- and lamin B1-specific siRNAs, showing transient NE rupture. Bar: 10 μ m. See also Video 10. (B) Quantification of cells from A, indicating the percentage of cells showing transient NE rupture when transfected with siCTL or siPar3 before lamina protein depletion (means \pm SEM [$n = 4$]; ****, $P < 0.0001$; ns, not significant). (C) Representative IB of lamin A/C, lamin B1, and Par3 depletion, as estimated by loading increasing amounts of control cell extracts (siCTL 1, 1/2, and 1/4); the graph shows quantification of Par3 and lamin protein levels (means \pm SEM [$n = 4$]). The relative knockdown in each condition is calculated relative to the siCTL condition. (D and E) Working model on the role of Par3 and the LINC complex in controlling the spatial dynamics of actin filaments and force transmission to the nucleus in response to E4orf4. See Discussion for more details.

MDA-MB-468 ($1.8 \times 10^5/2$ ml), HaCaT ($2 \times 10^5/2$ ml), and hTERT RPE-1 ($1.3 \times 10^5/2$ ml) cells were transferred to a 5-ml tube and gently mixed with Ad and/or baculovirus particles. CellLight reagents were added at four particles per cell. HeLa, U2OS, MDA-MB-231, MDA-MB-468, HaCaT and hTERT RPE-1 cells were infected with Ad-RFP (15 PFU/cell; completed with 60 PFU/cell Ad-LacZ) or Ad-E4orf4-mCherry (WT or GGG; 75 PFU/cell); 22Rv1 was infected with Ad-RFP (2 PFU/cell; completed with 18 PFU/cell Ad-LacZ) or Ad-E4orf4-mCherry (20 PFU/cell). The cell-virus suspensions were incubated at 37°C with light agitation for 15–30 min, seeded on 35-mm Petri dishes and incubated at 37°C. Culture medium was changed 16–20 h after infection. For shRNA knockdown, U2OS ($1.5 \times 10^5/2$ ml) cells were infected with lentiviral particles in the presence of 8 µg/ml polybrene. 48 h after infection, cells were replated, and selection of lentivirus-infected cells was performed by adding puromycin (1 µg/ml) for 48 h at 37°C. The resulting cells were harvested and infected with Ad-E4orf4 or Ad-RFP (96 h after infection with lentivirus-shRNA). The MISSION Par3-specific shRNA transduction particles were as follows: shPar3A, reference TRCN0000118134; sequence, 5'-CCGGCCATCGACAAATCTTATGATCTCGAGATCATAAGATTTGTCGATGGCTTTTTG; shPar3B, 5'-CCGGCCATCGACAAATCTTATGATACTCGAGTATCATAAGATTGTCGATGGTTTTG-3'.

Proliferation and cell death assay

To measure long-term survival by colony-forming assay tests, MCF10A (3.5×10^5) and MDA-MB-231 (2.8×10^5) cells were infected with Ad-GFP as control or Ad-Flag-E4orf4 at varying PFUs per cell (20, 40–50, 75–100 PFU/cell) in 35-mm Petri dishes. The culture medium was changed 16 h after infection, and duplicate cultures were harvested 24 h after infection for Western blot analyses. 40 h after infection, the cells were trypsinized, counted, and replated in each of three 60-mm Petri dishes at 2×10^4 , 2×10^2 , and 1×10^2 for each condition (technical replicates). The cells were grown at 37°C for 2 wk, and the resulting colonies were fixed in methanol/acetic acid (3:1), stained in a solution of 0.25% Trypan blue in 5% acetic acid, and scored manually. Cell proliferation and death were assessed from estimations of cell numbers according to a Trypan blue dye exclusion assay. At 24, 48, and 72 h after infection, the culture medium containing dying cells was recovered in a 5 ml-tube together with trypsinized adherent cells. The cell suspension was gently mixed with Trypan blue (0.4% in PBS 1X) at a 1:1 ratio and then rapidly counted in a hemacytometer. Each cell count was performed three to five times using independent Trypan blue cell suspension mixtures from the same sample for statistical reproducibility. White, refringent cells were considered viable, whereas dark, blue cells that incorporated the dye were considered nonviable.

Immunoprecipitation and Western blot experiments

Cells were suspended in their culture medium, pelleted, and washed with PBS. The cell pellet was lysed in 500 µl of 1% digitonin lysis buffer (0.1 M MES-NaOH, pH 6.5, 1 mM magnesium acetate, 0.5 mM EGTA, 200 µM sodium orthovanadate, and 1% digitonin with protease inhibitors [Roche; 1X Complete]; Fig. 2, B–D; and Fig. 5 C). Alternatively, cells were lysed by three

freeze-thaw cycles in 500 µl lysis buffer B (20 mM Tris-HCl, pH 7.6, 150 mM NaCl, 1 mM EDTA, 0.1% octylphenoxy poly(ethyleneoxy)ethanol (IGEPAL), 1 mM Na_3VO_4 , 10 mM NaF, 40 mM β -glycerophosphate, 1X Complete [Roche], and 1 mM DTT; Fig. S2, B and E). Lysates were centrifuged at 10,000 *g* for 15 min at 4°C in 1.5-ml tubes, and the supernatant was transferred to a new tube. Lysates were then precleared with 20 µl Dynabeads protein G (Life Technologies) for 30 min at 4°C. 20 µl Dynabeads protein G were incubated with 5 µg anti-Flag M2 (Sigma-Aldrich) or 1 µg anti-GFP (Molecular Probes) antibody in 500 µl lysis buffer for 30 min at 4°C. The lysate was then incubated with Dynabeads protein G for 1 h at 4°C with gentle agitation. Immune complexes were collected using a magnetic stand (EMD Millipore), washed three times in lysis buffer, and transferred to a fresh tube. Equal amounts of IPs were resolved by SDS-PAGE and analyzed by Western blot. Protein levels were determined after lysing cells in SDS sample buffer (62.5 mM Tris-HCl, pH 6.8, 2.3% SDS, 10% glycerol, 5% B-mercaptoethanol, 0.05% bromophenol blue, and 1 mM phenylmethylsulfonyl fluoride) and protein concentrations were measured using the DC protein assay reagent (Bio-Rad). Immunoblotting was performed as described previously (Lavoie et al., 2000).

AP-MS experiments

For AP-MS experiments, MDA-MB-231 cells plated on 150-mm Petri dishes (eight dishes per condition), were infected with Ad-Flag-E4orf4-mCherry or control Ad-lacZ recombinant Ads (75 PFUs/cell). Cells were collected and lysed in digitonin buffer 16 h after infection. IP was performed using anti-Flag M2 antibody, and proteins were eluted using the Flag peptide (100 µg/ml), overnight at 4°C. The eluate was collected and concentrated on a Vivaspin 500 Protein Concentrator 10-kD Column (GE Healthcare Life Sciences) and then diluted into the appropriate amount of 3X SDS sample buffer. The eluate and the Dynabeads in SDS-sample buffer were loaded on a 6–10% gradient polyacrylamide gel and allowed to migrate until the migration front reached 10 cm. The gel was stained with Coomassie blue (50% methanol vol/vol, 10% acetic acid vol/vol, and 0.1% Coomassie blue wt/vol) and washed in destaining solution (10% methanol vol/vol and 10% acetic acid vol/vol) overnight at RT. Bands of interest were extracted from small pieces of gels that had been cut to cover all protein samples and placed in 96-well plates and then processed for MS/MS analyses. Each AP-MS experiment was performed in biological triplicate ($n = 3$) to perform SAINT analyses, as reported previously (Choi et al., 2011, 2012), using Flag controls to filtrate background contaminants.

Mass spectrometry was performed by the Proteomics platform of the CR-CHU de Québec Université Laval on a TripleTOF 5600 (AB Sciex) mass spectrometer equipped with an ion source (NanoSpray III; AB Sciex) and coupled to a nanopump and by the Proteomics And Bioanalytical Mass Spectrometry of the Institute for Research in Immunology and Cancer (Montreal University, Quebec, Canada) on a quadrupole/TOF Q-STAR (AB Sciex) mass spectrometer. MS/MS samples were analyzed using Mascot (Matrix Science) that was set up to search the UR100_12_05_-Homo_sapiens_9606 database (128,347 entries), with a fragment ion mass tolerance of 0.50 D and a parent ion tolerance of 2.0 D.

Scaffold (version Scaffold_4.8.4, Proteome Software Inc., Portland, OR) was used to validate MS/MS based peptide and protein identifications. Peptide identifications were accepted if established at greater than 95% probability to achieve a maximum of 1.2% false discovery rate. Protein identifications were accepted if they contained at least two identified peptides. Peptide and protein probabilities were assigned by the Protein Prophet algorithm.

Immunofluorescence, PLA, and microscopic analyses

Cells plated on fibronectin-coated glass coverslips (Thermo Fisher Scientific; No. 1.5) were fixed with 4% paraformaldehyde (Bio Basics) for 20 min at RT. DNA was stained with cell-permeable Hoechst. Cells were permeabilized with 0.2% Triton X-100 in PBS containing 1 mM MgCl₂ for 15 min at RT. F-actin was stained with a 1/100 dilution of Alexa-Fluor phalloidin in PBS for 20 min at RT. Immunostaining of proteins was performed as described previously (Lavoie et al., 2000), and coverslips were mounted on glass slides using the ProLong Glass Antifade Mountant (Invitrogen; P36980). PLA detection was performed according to the manufacturer's instructions using PBS containing 5% milk and 1 mM MgCl₂ as a blocking solution. Antibodies (anti-Par3 diluted at 1/100 and anti-HA diluted at 1/500) were incubated in PBS supplemented with 1% milk and 1 mM MgCl₂. Volocity software was used to count the number of PLA foci per cell after background subtraction using the "Find objects" tool in the Measurements thumbnail. Detection was according to intensity using an intensity threshold set to optimally detect the foci, minimal object size = 0.3 μm³, and "Separate touching objects" (object size guide = 0.3 μm³).

Cell blebbing and nuclear condensation were quantified by visual inspection of fixed specimens using an AxioObserver Z1 system with a 60× oil 1.25 NA objective and an AxioCam MRm charged-coupled device camera controlled by Zen software (Carl Zeiss). Cell blebbing was determined by phalloidin staining, and nuclear condensation was scored based on a decreased nuclear surface with condensed chromatin, as visualized by Hoechst staining. N/C intensity ratio and nuclear circularity index were measured on confocal images acquired with a PerkinElmer UltraVIEW spinning disk confocal (60× oil 1.4 NA) equipped with an Hamamatsu C9100-50 Electron Multiplier EMCCD camera at -50°C driven the Volocity software version 6.3 (Quorum Technologies), or with an Orca Flash 4.0LT+ sCMOS camera (Hamamatsu Photonics K.K.) driven by the NIS Elements software version 5.02.00 (Nikon.ca). The N/C ratio was estimated from the mean fluorescence intensity of the nuclear surface relative to the cytoplasmic surface, as delineated on the median confocal plane using Volocity software version 6.3 or Fiji software (ImageJ 2.0.0-rc-69/1.52n). The nuclear circularity index was estimated from maximum intensity projection images of lamin A/C-stained cells using the "shape descriptor" tool of Fiji software (ImageJ 2.0.0-rc-69/1.52n). Image processing was done using Fiji software and was limited to background subtraction, brightness and contrast adjustment, and deconvolution using Volocity software, when indicated.

High-resolution confocal imaging of Par3 and lamin A/C staining on fixed cells was performed using a 63×/1.4 C-Plan Apo oil-immersion lens on a Zeiss LSM 800 microscope in Airyscan

mode. Image acquisition and processing of Airyscan datasets was performed with the Zen Blue 2.6 software. For Par3 cluster analysis, the Fiji software (ImageJ 2.0.0-rc-69/1.52n) was used to apply an Intermode threshold, and a region of interest was then manually drawn to encompass each cell. The area of all clusters was quantified by using the "analyze particles" tool. No size or circularity limitation was included. Par3 and lamin A/C intensity profiles were analyzed using the plot profile tool of Fiji software (ImageJ 2.0.0-rc-69/1.52n).

Live-cell imaging

Confocal microscopy of live cells was performed with a PerkinElmer UltraVIEW spinning disk confocal (40× oil 1.3 NA, or 40× 0.75 NA, or 20× 0.50 NA), equipped with a humidified, 5% CO₂ thermoregulated chamber. Cells were plated on fibronectin-coated glass dishes (Corning; Fluorodish) the day before transfection or infection. For E4orf4-induced nuclear bleb formation, NE rupture, and actin structure dynamics, cells were imaged after release from a 2-h treatment with blebbistatin (50 μM); imaging was performed at 7 h after transfection of HeLa cells with Flag-E4orf4-mRFP or 20 h after infection of U2OS or MDA-MB-468 cells with Ad-RFP, Ad-GFP, and Ad-Flag-E4orf4-mCherry, with or without CellLight Nucleus-GFP, BacMam 2.0, or Ad-LifeAct-GFP. Where required, cells were transfected with siRNAs or infected with lentivirus shRNAs at least 48 h before transfection or infection with E4orf4 constructs. Images (multiple fields/sample) were acquired at 5-, 1.5-, or 1-min intervals for 3–12 h. Analysis of actin structure dynamics was performed on maximum intensity projections of image stacks from time-lapse movies using MATLAB and ImageJ. A median filter was applied to the image stacks (1-pixel radius), and a line (5 pixels wide) was drawn perpendicular to actin network and across the nucleus over the width of the cell. A kymograph was extracted along the drawn line for both the actin and E4orf4 fluorescence channels. The actin kymograph was then used to measure the speed at which actin fibers were translating within the cells by calculating the slope of the visible fiber components. The E4orf4 channel was then used as a reference of the nucleus position to establish the relative speed of actin structure. The time point 0 min corresponds to the beginning of cell recording, 24 h after recombinant virus transduction (64 h after siRNA transfection). All visible actin filaments, but not the cell cortex, were considered in the analysis. For analysis of spontaneous NE rupture induced by lamina protein depletion, HeLa cells plated at low confluency were transfected with Par3-specific siRNAs (50 nM), and 48 h later, the cell cultures were treated with a mixture of lamin A/C- and lamin-B1-specific siRNAs used at 15 nM to achieve moderate knockdowns and avoid toxicity (~20% lamina protein depletion). Concomitantly, cells were infected with a recombinant baculovirus encoding RFP-NLS overnight (CellLight Nucleus-RFP, BacMam 2.0). Cell imaging was started 16 h after lamin depletion, and images were recorded at 5-min intervals for 12 h.

Statistical analyses

For experiments examining the difference between two conditions, the mean values of individual experiments were

analyzed using the Mann–Whitney test, a nonparametric test suitable to compare two small unpaired groups of ordinal or numerical variables. For quantitative analyses examining the proportions of cells displaying phenotypes of membrane blebbing, nuclear condensation, nuclear bleb formation, NE rupture, and cell death, data were analyzed using the Fisher's exact test, which is used for small sample sizes with nominal/categorical variables. To analyze the difference in cell proliferation, statistical analysis was performed using the two-way ANOVA test. To analyze the difference in E4orf4 N/C ratio and nuclear circularity index, individual measurements for each cell were pooled together for each condition and analyzed using the Kruskal–Wallis test with Dunn's multiple comparisons, which is a nonparametric test suitable to compare several groups of numerical variables. For actin structure velocities, statistical significance was analyzed using a two-tailed Student's *t* test. Statistical calculations were performed using Prism 8.1.1 (GraphPad Software) statistical software. The significance of *P* values is shown as *, *P* < 0.05; **, *P* < 0.01; ***, *P* < 0.001; ****, *P* < 0.0001. In many cases of one or two independent experiments, data were collected in different nontumorigenic and tumorigenic cell models or from replicates of two or more independent siRNAs/shRNAs, adding robustness to the results. Phenotypic data were collected through the analysis of many fields to properly represent the entire sample, and technical counts for independent experiments were obtained by two independent investigators or repeated two or three times.

Data availability

Proteomic data have been deposited to the ProteomeXchange Consortium via the PRIDE partner repository (Vizcaíno et al., 2016) with the dataset identifier PXD014329. All data that support the findings of this study are available from the corresponding author upon reasonable request.

Online supplemental material

Fig. S1 shows representative images of transduction efficiencies and analysis of cell blebbing and determination of nuclear condensation phenotypes in cells from various origins expressing RFP alone or E4orf4-mCherry, showing the actomyosin-dependent tumor cell-selective effects of E4orf4. Fig. S2 shows structure–function analyses, supporting a requirement for Par3 binding and scaffolding function for E4orf4-induced cell blebbing and nuclear condensation in 293T cells. Fig. S3 A provides representative images of the PLA assay controls related to Fig. 4, C and D; Fig. S3 B shows the recruitment of atypical protein kinase C (aPKC) substrates at nuclear deformation sites. Fig. S3 C shows loss-of-function phenotypes of the E4orf4-GGG mutant. Fig. S4 A shows the efficiency of Par3 depletion in HeLa cells. Fig. S4, B and C show E4orf4 loss-of-function phenotypes upon depleting Par3 or SUN1/2. Fig. S5, A–C show the effects of dominant-negative KASH2 constructs on E4orf4 phenotypes in HeLa cells. Fig. S5 D shows Par3–GFP localization relative to F-actin in an E4orf4-expressing HeLa cell. Fig. S5 E shows Par3 depletion efficiency in single cells. Video 1 shows the distinctive dynamics of nuclear blebs in representative E4orf4-mRFP-expressing HeLa cells transfected

with siCTL or siPar3-3. Video 2 shows the absence of nuclear blebbing in control HeLa cells expressing mRFP-NLS. Video 3 shows a representative U2OS cell expressing E4orf4-mCherry undergoing nuclear bleb rupture and E4orf4 efflux. Video 4 shows a representative E4orf4-mCherry-expressing MDA-MB-468 cell undergoing repetitive cycles of nuclear bleb formations and ruptures along with E4orf4 signal effluxes. Videos 5 and 6 show representative HeLa and U2OS cells expressing E4orf4-mCherry undergoing NE rupture and repair. Videos 7, 8, and 9 show representative dynamics of actin filaments relative to nuclear rupture in U2OS cells expressing E4orf4-mCherry and GFP-LifeAct, showing that Par3 depletion inhibits the recruitment of actin filaments at the nuclear surface. Video 10 shows transient NE rupture after lamin depletion in HeLa cells.

Acknowledgments

We are grateful to Dr. E. Sahai (GFP-Par3 construct; Francis Crick Institute, London, UK), Dr. D. Hodzic (GFP-KASH2 and GFP-KASH2ext constructs; Washington University School of Medicine, MO), and Dr. Lee (GFP-NLS construct; University of Ottawa, Ottawa, Ontario, Canada) for kindly providing critical reagents. We thank Dr. N. Bisson for assistance in MS data significance analyses, C. St-Pierre for help with microscopic systems, and Sarah Côté for technical help. We thank Carl Zeiss Canada for the time on an LSM800 Airyscan on this study and arranging installation and application support.

This work was funded by the Natural Sciences and Engineering Research Council (Discovery grant RGPIN/05849 to J.N. Lavoie) and the Cancer Research Society (operating grant to J.N. Lavoie). J.N. Lavoie was also supported by the Canadian Institutes of Health Research (49450 and 7088 to J.N. Lavoie) and the Fondation CHU de Québec. C. Dziengelewski was supported by a doctoral award from the Fonds de Recherche Nature et Technologies du Québec. M.-A. Rodrigue and A. Caillier were supported by Fonds de la Recherche en Santé du Québec. F. Bordeleau holds a Fonds de la Recherche en Santé du Québec Research Scholar Junior 1 salary award, and M.-E. Huot holds a Fonds de la Recherche en Santé du Québec Research Scholar Junior 2 salary award.

The authors declare no competing financial interests.

Author contributions: C. Dziengelewski, M.-A. Rodrigue, M.-C. Boulanger, and J.N. Lavoie conceptualized the research; C. Dziengelewski, M.-A. Rodrigue, M.-C. Boulanger, A. Caillier, J. Bergeman, M. Fuchs, H. Lambert, and J.N. Lavoie investigated and performed formal analyses; F. Bordeleau, M.E. Huot, P. Laprise, and D.E. Richard provided essential expertise or resources; C. Dziengelewski, M.-A. Rodrigue, M.-C. Boulanger, K. Jacquet, A. Caillier, F. Bordeleau, and J.N. Lavoie analyzed data; C. Dziengelewski, M.-A. Rodrigue, K. Jacket, and F. Bordeleau prepared figures; C. Dziengelewski, M.-A. Rodrigue, and J.N. Lavoie wrote the paper; and D.E. Richard edited the manuscript.

Submitted: 22 May 2018

Revised: 12 December 2019

Accepted: 4 February 2020

References

- Alibert, C., B. Goud, and J.B. Manneville. 2017. Are cancer cells really softer than normal cells? *Biol. Cell.* 109:167–189. <https://doi.org/10.1111/boc.201600078>
- Alvarado-Kristensson, M., and C.A. Rosselló. 2019. The Biology of the Nuclear Envelope and Its Implications in Cancer Biology. *Int. J. Mol. Sci.* 20: E2586. <https://doi.org/10.3390/ijms20102586>
- Bergeman, J., A. Caillier, F. Houle, L.M. Gagné, and M.E. Huot. 2016. Localized translation regulates cell adhesion and transendothelial migration. *J. Cell Sci.* 129:4105–4117.
- Bodnar, A.G., M. Ouellette, M. Frollis, S.E. Holt, C.P. Chiu, G.B. Morin, C.B. Harley, J.W. Shay, S. Lichtsteiner, and W.E. Wright. 1998. Extension of life-span by introduction of telomerase into normal human cells. *Science.* 279:349–352. <https://doi.org/10.1126/science.279.5349.349>
- Boukamp, P., R.T. Petrussevska, D. Breitkreutz, J. Hornung, A. Markham, and N.E. Fusenig. 1988. Normal keratinization in a spontaneously immortalized aneuploid human keratinocyte cell line. *J. Cell Biol.* 106:761–771. <https://doi.org/10.1083/jcb.106.3.761>
- Calero-Cuenca, F.J., C.S. Janota, and E.R. Gomes. 2018. Dealing with the nucleus during cell migration. *Curr. Opin. Cell Biol.* 50:35–41. <https://doi.org/10.1016/j.ceb.2018.01.014>
- Champagne, C., M.C. Landry, M.C. Gingras, and J.N. Lavoie. 2004. Activation of adenovirus type 2 early region 4 ORF4 cytoplasmic death function by direct binding to Src kinase domain. *J. Biol. Chem.* 279:25905–25915. <https://doi.org/10.1074/jbc.M400933200>
- Choi, H., B. Larsen, Z.Y. Lin, A. Breitkreutz, D. Mellacheruvu, D. Fermin, Z.S. Qin, M. Tyers, A.C. Gingras, and A.I. Nesvizhskii. 2011. SAINT: probabilistic scoring of affinity purification-mass spectrometry data. *Nat. Methods.* 8:70–73. <https://doi.org/10.1038/nmeth.1541>
- Choi, H., G. Liu, D. Mellacheruvu, M. Tyers, A.C. Gingras, and A.I. Nesvizhskii. 2012. Analyzing protein-protein interactions from affinity purification-mass spectrometry data with SAINT. *Curr. Protoc. Bioinformatics.* Chapter 8:Unit8.15.
- De Vos, W.H., F. Houben, M. Kamps, A. Malhas, F. Verheyen, J. Cox, E.M. Manders, V.L. Verstraeten, M.A. van Steensel, C.L. Marcelis, et al. 2011. Repetitive disruptions of the nuclear envelope invoke temporary loss of cellular compartmentalization in laminopathies. *Hum. Mol. Genet.* 20: 4175–4186. <https://doi.org/10.1093/hmg/ddr344>
- Debnath, J., S.K. Muthuswamy, and J.S. Brugge. 2003. Morphogenesis and oncogenesis of MCF-10A mammary epithelial acini grown in three-dimensional basement membrane cultures. *Methods.* 30:256–268. [https://doi.org/10.1016/S1046-2023\(03\)00032-X](https://doi.org/10.1016/S1046-2023(03)00032-X)
- Delorme-Axford, E., and C.B. Coyne. 2011. The actin cytoskeleton as a barrier to virus infection of polarized epithelial cells. *Viruses.* 3:2462–2477. <https://doi.org/10.3390/v3122462>
- Denais, C., and J. Lammerding. 2014. Nuclear mechanics in cancer. *Adv. Exp. Med. Biol.* 773:435–470. https://doi.org/10.1007/978-1-4899-8032-8_20
- Denais, C.M., R.M. Gilbert, P. Isermann, A.L. McGregor, M. te Lindert, B. Weigelin, P.M. Davidson, P. Friedl, K. Wolf, and J. Lammerding. 2016. Nuclear envelope rupture and repair during cancer cell migration. *Science.* 352:353–358. <https://doi.org/10.1126/science.aad7297>
- Facciuto, F., M. Bugnon Valdano, F. Marziali, P. Massimi, L. Banks, A.L. Cavatorta, and D. Gardiol. 2014. Human papillomavirus (HPV)-18 E6 oncoprotein interferes with the epithelial cell polarity Par3 protein. *Mol. Oncol.* 8:533–543. <https://doi.org/10.1016/j.molonc.2014.01.002>
- Fedorchak, G.R., A. Kaminski, and J. Lammerding. 2014. Cellular mechanosensing: getting to the nucleus of it all. *Prog. Biophys. Mol. Biol.* 115:76–92. <https://doi.org/10.1016/j.pbiomolbio.2014.06.009>
- Fogg, V.C., C.J. Liu, and B. Margolis. 2005. Multiple regions of Crumbs3 are required for tight junction formation in MCF10A cells. *J. Cell Sci.* 118: 2859–2869. <https://doi.org/10.1126/jcs.02412>
- Foster, C.R., S.A. Przyborski, R.G. Wilson, and C.J. Hutchison. 2010. Lamins as cancer biomarkers. *Biochem. Soc. Trans.* 38:297–300. <https://doi.org/10.1042/BST0380297>
- Friedl, P., K. Wolf, and J. Lammerding. 2011. Nuclear mechanics during cell migration. *Curr. Opin. Cell Biol.* 23:55–64. <https://doi.org/10.1016/j.ceb.2010.10.015>
- Gandalovičová, A., T. Vomasťek, D. Rosel, and J. Brábek. 2016. Cell polarity signaling in the plasticity of cancer cell invasiveness. *Oncotarget.* 7: 25022–25049. <https://doi.org/10.18632/oncotarget.7214>
- Goldstein, B., and I.G. Macara. 2007. The PAR proteins: fundamental players in animal cell polarization. *Dev. Cell.* 13:609–622. <https://doi.org/10.1016/j.devcel.2007.10.007>
- Guilluy, C., L.D. Osborne, L. Van Landeghem, L. Sharek, R. Superfine, R. Garcia-Mata, and K. Burridge. 2014. Isolated nuclei adapt to force and reveal a mechanotransduction pathway in the nucleus. *Nat. Cell Biol.* 16: 376–381. <https://doi.org/10.1038/ncb2927>
- Halaoui, R., and L. McCaffrey. 2015. Rewiring cell polarity signaling in cancer. *Oncogene.* 34:939–950. <https://doi.org/10.1038/onc.2014.59>
- Hatch, E.M., and M.W. Hetzer. 2016. Nuclear envelope rupture is induced by actin-based nucleus confinement. *J. Cell Biol.* 215:27–36. <https://doi.org/10.1083/jcb.201603053>
- Hatch, E.M., A.H. Fischer, T.J. Deerinck, and M.W. Hetzer. 2013. Catastrophic nuclear envelope collapse in cancer cell micronuclei. *Cell.* 154:47–60. <https://doi.org/10.1016/j.cell.2013.06.007>
- Hidalgo-Carcedo, C., S. Hooper, S.I. Chaudhry, P. Williamson, K. Harrington, B. Leitinger, and E. Sahai. 2011. Collective cell migration requires suppression of actomyosin at cell-cell contacts mediated by DDR1 and the cell polarity regulators Par3 and Par6. *Nat. Cell Biol.* 13:49–58. <https://doi.org/10.1038/ncb2133>
- Iden, S., W.E. van Riel, R. Schäfer, J.Y. Song, T. Hirose, S. Ohno, and J.G. Collard. 2012. Tumor type-dependent function of the par3 polarity protein in skin tumorigenesis. *Cancer Cell.* 22:389–403. <https://doi.org/10.1016/j.ccr.2012.08.004>
- Isermann, P., and J. Lammerding. 2017. Consequences of a tight squeeze: Nuclear envelope rupture and repair. *Nucleus.* 8:268–274. <https://doi.org/10.1080/19491034.2017.1292191>
- Kleinberger, T. 2014. Induction of cancer-specific cell death by the adenovirus E4orf4 protein. *Adv. Exp. Med. Biol.* 818:61–97. https://doi.org/10.1007/978-1-4471-6458-6_4
- Kraning-Rush, C.M., J.P. Califano, and C.A. Reinhart-King. 2012. Cellular traction stresses increase with increasing metastatic potential. *PLoS One.* 7:e32572. <https://doi.org/10.1371/journal.pone.0032572>
- Lammerding, J., P.C. Schulze, T. Takahashi, S. Kozlov, T. Sullivan, R.D. Kamm, C.L. Stewart, and R.T. Lee. 2004. Lamin A/C deficiency causes defective nuclear mechanics and mechanotransduction. *J. Clin. Invest.* 113:370–378. <https://doi.org/10.1172/JCI200419670>
- Landry, M.C., A. Sicotte, C. Champagne, and J.N. Lavoie. 2009. Regulation of cell death by recycling endosomes and golgi membrane dynamics via a pathway involving Src-family kinases, Cdc42 and Rab11a. *Mol. Biol. Cell.* 20:4091–4106. <https://doi.org/10.1091/mbc.e09-01-0057>
- Landry, M.C., C. Champagne, M.C. Boulanger, A. Jetté, M. Fuchs, C. Dziengielewski, and J.N. Lavoie. 2014. A functional interplay between the small GTPase Rab11a and mitochondria-shaping proteins regulates mitochondrial positioning and polarization of the actin cytoskeleton downstream of Src family kinases. *J. Biol. Chem.* 289:2230–2249. <https://doi.org/10.1074/jbc.M113.516351>
- Lavoie, J.N., M. Nguyen, R.C. Marcellus, P.E. Branton, and G.C. Shore. 1998. E4orf4, a novel adenovirus death factor that induces p53-independent apoptosis by a pathway that is not inhibited by zVAD-fmk. *J. Cell Biol.* 140:637–645. <https://doi.org/10.1083/jcb.140.3.637>
- Lavoie, J.N., C. Champagne, M.C. Gingras, and A. Robert. 2000. Adenovirus E4 open reading frame 4-induced apoptosis involves dysregulation of Src family kinases. *J. Cell Biol.* 150:1037–1056. <https://doi.org/10.1083/jcb.150.5.1037>
- Lavoie, J.N., M.C. Landry, R.L. Faure, and C. Champagne. 2010. Src-family kinase signaling, actin-mediated membrane trafficking and organellar dynamics in the control of cell fate: lessons to be learned from the adenovirus E4orf4 death factor. *Cell. Signal.* 22:1604–1614. <https://doi.org/10.1016/j.cellsig.2010.04.007>
- Le Berre, M., J. Aubertin, and M. Piel. 2012. Fine control of nuclear confinement identifies a threshold deformation leading to lamina rupture and induction of specific genes. *Integr. Biol.* 4:1406–1414.
- Lele, T.P., R.B. Dickinson, and G.G. Gundersen. 2018. Mechanical principles of nuclear shaping and positioning. *J. Cell Biol.* 217:3330–3342. <https://doi.org/10.1083/jcb.201804052>
- Liu, L., Q. Luo, J. Sun, and G. Song. 2016. Nucleus and nucleus-cytoskeleton connections in 3D cell migration. *Exp. Cell Res.* 348:56–65. <https://doi.org/10.1016/j.yexcr.2016.09.001>
- Livne, A., R. Shtrichman, and T. Kleinberger. 2001. Caspase activation by adenovirus e4orf4 protein is cell line specific and is mediated by the death receptor pathway. *J. Virol.* 75:789–798. <https://doi.org/10.1128/JVI.75.2.789-798.2001>
- Lombardi, M.L., and J. Lammerding. 2011. Keeping the LINC: the importance of nucleocytoskeletal coupling in intracellular force transmission and cellular function. *Biochem. Soc. Trans.* 39:1729–1734. <https://doi.org/10.1042/BST20110686>
- Mack, N.A., and M. Georgiou. 2014. The interdependence of the Rho GTPases and apical-basal cell polarity. *Small GTPases.* 5: e973768. <https://doi.org/10.4161/21541248.2014.973768>

- Marcellus, R.C., H. Chan, D. Paquette, S. Thirlwell, D. Boivin, and P.E. Branton. 2000. Induction of p53-independent apoptosis by the adenovirus E4orf4 protein requires binding to the Balph subunit of protein phosphatase 2A. *J. Virol.* 74:7869–7877. <https://doi.org/10.1128/JVI.74.17.7869-7877.2000>
- Mohammadi, H., and E. Sahai. 2018. Mechanisms and impact of altered tumour mechanics. *Nat. Cell Biol.* 20:766–774. <https://doi.org/10.1038/s41556-018-0131-2>
- Mui, M.Z., Y. Zhou, P. Blanchette, N. Chughtai, J.F. Knight, T. Grusso, A.I. Papadakis, S. Huang, M. Park, A.C. Gingras, and P.E. Branton. 2015. The Human Adenovirus Type 5 E4orf4 Protein Targets Two Phosphatase Regulators of the Hippo Signaling Pathway. *J. Virol.* 89:8855–8870. <https://doi.org/10.1128/JVI.03710-14>
- Munro, E. 2017. Protein Clustering Shapes Polarity Protein Gradients. *Dev. Cell.* 42:309–311. <https://doi.org/10.1016/j.devcel.2017.08.006>
- Nance, J., and J.A. Zallen. 2011. Elaborating polarity: PAR proteins and the cytoskeleton. *Development.* 138:799–809. <https://doi.org/10.1242/dev.053538>
- Neve, R.M., K. Chin, J. Fridlyand, J. Yeh, F.L. Baehner, T. Fevr, L. Clark, N. Bayani, J.P. Coppe, F. Tong, et al. 2006. A collection of breast cancer cell lines for the study of functionally distinct cancer subtypes. *Cancer Cell.* 10:515–527. <https://doi.org/10.1016/j.ccr.2006.10.008>
- Neveu, B., P. Jain, B. Têtu, L. Wu, Y. Fradet, and F. Pouliot. 2016. A PCA3 gene-based transcriptional amplification system targeting primary prostate cancer. *Oncotarget.* 7:1300–1310. <https://doi.org/10.18632/oncotarget.6360>
- Nürnberg, A., T. Kitzing, and R. Grosse. 2011. Nucleating actin for invasion. *Nat. Rev. Cancer.* 11:177–187. <https://doi.org/10.1038/nrc3003>
- Ooshio, T., N. Fujita, A. Yamada, T. Sato, Y. Kitagawa, R. Okamoto, S. Nakata, A. Miki, K. Irie, and Y. Takai. 2007. Cooperative roles of Par-3 and afadin in the formation of adherens and tight junctions. *J. Cell Sci.* 120:2352–2365. <https://doi.org/10.1242/jcs.03470>
- Paszek, M.J., N. Zahir, K.R. Johnson, J.N. Lakin, G.I. Rozenberg, A. Gefen, C.A. Reinhart-King, S.S. Margulies, M. Dembo, D. Boettiger, et al. 2005. Tensional homeostasis and the malignant phenotype. *Cancer Cell.* 8:241–254. <https://doi.org/10.1016/j.ccr.2005.08.010>
- Raab, M., M. Gentili, H. de Belly, H.R. Thiam, P. Vargas, A.J. Jimenez, F. Lautenschlaeger, R. Voituriez, A.M. Lennon-Duménil, N. Manel, and M. Piel. 2016. ESCRT III repairs nuclear envelope ruptures during cell migration to limit DNA damage and cell death. *Science.* 352:359–362. <https://doi.org/10.1126/science.aad7611>
- Robert, A., M.J. Miron, C. Champagne, M.C. Gingras, P.E. Branton, and J.N. Lavoie. 2002. Distinct cell death pathways triggered by the adenovirus early region 4 ORF 4 protein. *J. Cell Biol.* 158:519–528. <https://doi.org/10.1083/jcb.200201106>
- Robert, A., N. Smadja-Lamère, M.C. Landry, C. Champagne, R. Petrie, N. Lamarche-Vane, H. Hosoya, and J.N. Lavoie. 2006. Adenovirus E4orf4 hijacks rho GTPase-dependent actin dynamics to kill cells: a role for endosome-associated actin assembly. *Mol. Biol. Cell.* 17:3329–3344. <https://doi.org/10.1091/mbc.e05-12-1146>
- Robijns, J., F. Molenberghs, T. Sieprath, T.D. Corne, M. Verschuuren, and W.H. De Vos. 2016. In silico synchronization reveals regulators of nuclear ruptures in lamin A/C deficient model cells. *Sci. Rep.* 6:30325. <https://doi.org/10.1038/srep30325>
- Rosen, H., R. Sharf, A. Pechkovsky, A. Salzberg, and T. Kleinberger. 2019. Selective elimination of cancer cells by the adenovirus E4orf4 protein in a Drosophila cancer model: a new paradigm for cancer therapy. *Cell Death Dis.* 10:455. <https://doi.org/10.1038/s41419-019-1680-4>
- Sedgwick, G.G., D.G. Hayward, B. Di Fiore, M. Pardo, L. Yu, J. Pines, and J. Nilsson. 2013. Mechanisms controlling the temporal degradation of Nek2A and Kif18A by the APC/C-Cdc20 complex. *EMBO J.* 32:303–314. <https://doi.org/10.1038/emboj.2012.335>
- Shah, P., K. Wolf, and J. Lammerding. 2017. Bursting the Bubble - Nuclear Envelope Rupture as a Path to Genomic Instability? *Trends Cell Biol.* 27:546–555. <https://doi.org/10.1016/j.tcb.2017.02.008>
- Shtrichman, R., and T. Kleinberger. 1998. Adenovirus type 5 E4 open reading frame 4 protein induces apoptosis in transformed cells. *J. Virol.* 72:2975–2982. <https://doi.org/10.1128/JVI.72.4.2975-2982.1998>
- Shtrichman, R., R. Sharf, H. Barr, T. Dobner, and T. Kleinberger. 1999. Induction of apoptosis by adenovirus E4orf4 protein is specific to transformed cells and requires an interaction with protein phosphatase 2A. *Proc. Natl. Acad. Sci. USA.* 96:10080–10085. <https://doi.org/10.1073/pnas.96.18.10080>
- Smadja-Lamère, N., M.C. Boulanger, C. Champagne, P.E. Branton, and J.N. Lavoie. 2008. JNK-mediated phosphorylation of paxillin in adhesion assembly and tension-induced cell death by the adenovirus death factor E4orf4. *J. Biol. Chem.* 283:34352–34364. <https://doi.org/10.1074/jbc.M803364200>
- Stewart-Hutchinson, P.J., C.M. Hale, D. Wirtz, and D. Hodzic. 2008. Structural requirements for the assembly of LINC complexes and their function in cellular mechanical stiffness. *Exp. Cell Res.* 314:1892–1905. <https://doi.org/10.1016/j.yexcr.2008.02.022>
- Straight, A.F., A. Cheung, J. Limouze, I. Chen, N.J. Westwood, J.R. Sellers, and T.J. Mitchison. 2003. Dissecting temporal and spatial control of cytokinesis with a myosin II inhibitor. *Science.* 299:1743–1747. <https://doi.org/10.1126/science.1081412>
- Taylor, M.P., O.O. Koyuncu, and L.W. Enquist. 2011. Subversion of the actin cytoskeleton during viral infection. *Nat. Rev. Microbiol.* 9:427–439. <https://doi.org/10.1038/nrmicro2574>
- Van den Broeke, C., T. Jacob, and H.W. Favoreel. 2014. Rho'ing in and out of cells: viral interactions with Rho GTPase signaling. *Small GTPases.* 5:e28318. <https://doi.org/10.4161/sgtp.28318>
- Vargas, J.D., E.M. Hatch, D.J. Anderson, and M.W. Hetzer. 2012. Transient nuclear envelope rupturing during interphase in human cancer cells. *Nucleus.* 3:88–100. <https://doi.org/10.4161/nucl.18954>
- Vizcaíno, J.A., A. Csordas, N. Del-Toro, J.A. Dienes, J. Griss, I. Lavidas, G. Mayer, Y. Perez-Riverol, F. Reisinger, T. Ternent, et al. 2016. 2016 update of the PRIDE database and its related tools. *Nucleic Acids Res.* 44:11033. <https://doi.org/10.1093/nar/gkw880>
- Xue, B., K. Krishnamurthy, D.C. Allred, and S.K. Muthuswamy. 2013. Loss of Par3 promotes breast cancer metastasis by compromising cell-cell cohesion. *Nat. Cell Biol.* 15:189–200. <https://doi.org/10.1038/ncb2663>
- Zanotelli, M., F. Bordeleau, and C.A. Reinhart-King. 2018. Subcellular regulation of cancer cell mechanics. *Curr. Opin. Biomed. Eng.* 1:8–14.

Supplemental material

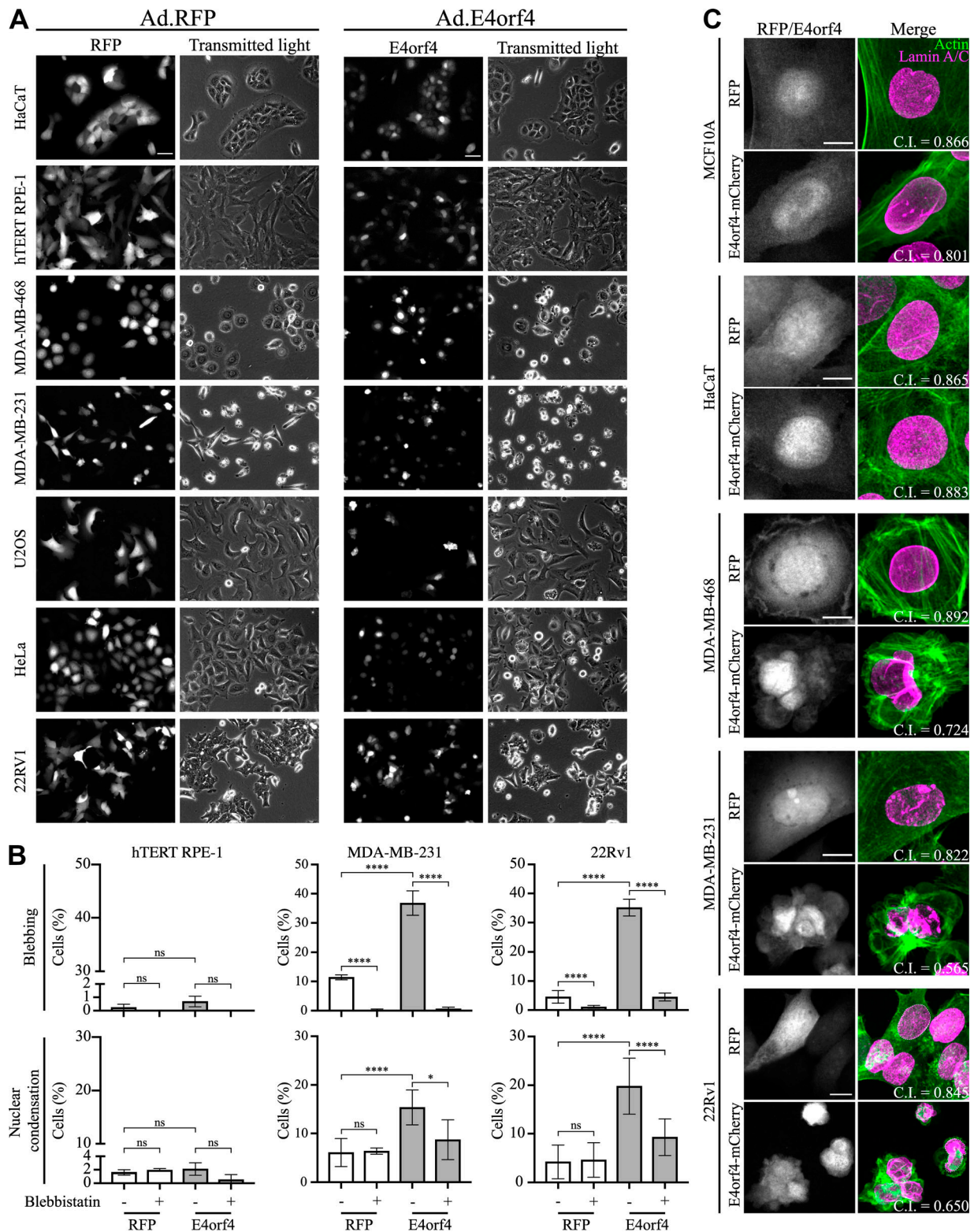


Figure S1. **Supporting information related to the tumor cell-selective E4orf4 phenotypes in cell lines of various origins.** (A) Representative epifluorescence images of cells from various origins transduced with Ad-RFP or Ad-E4orf4-mCherry, showing transduction efficiencies 48 h after transduction, associated with the absence (nontumorigenic cells: HaCaT and hTERT RPE-1) or presence (cancer cell lines: MDA-MB-468, MDA-MB-231, U2OS, HeLa, and 22RV1) of morphological changes (cell rounding and blebbing). Bars: 50 μ m. (B) Quantification of the percentage of cell blebbing and nuclear condensation cell, as scored relative to cells expressing RFP/E4orf4-mCherry 24–36 h after transduction, before and after blebbistatin treatment (50 μ M, 2 h), for datasets represented in C (means \pm SEM [$n \geq 3$]; *, $P < 0.05$; ****, $P < 0.0001$; ns, not significant). (C) Maximum intensity projections of confocal image stacks of representative RFP- or E4orf4-mCherry-expressing cells; the nuclear circularity index (C.I.) was measured from lamin A/C staining; for the 22RV1 cell panel, the indicated circularity index corresponds to the nucleus designated by a dotted white line. ns, not significant. Bars, 10 μ m.

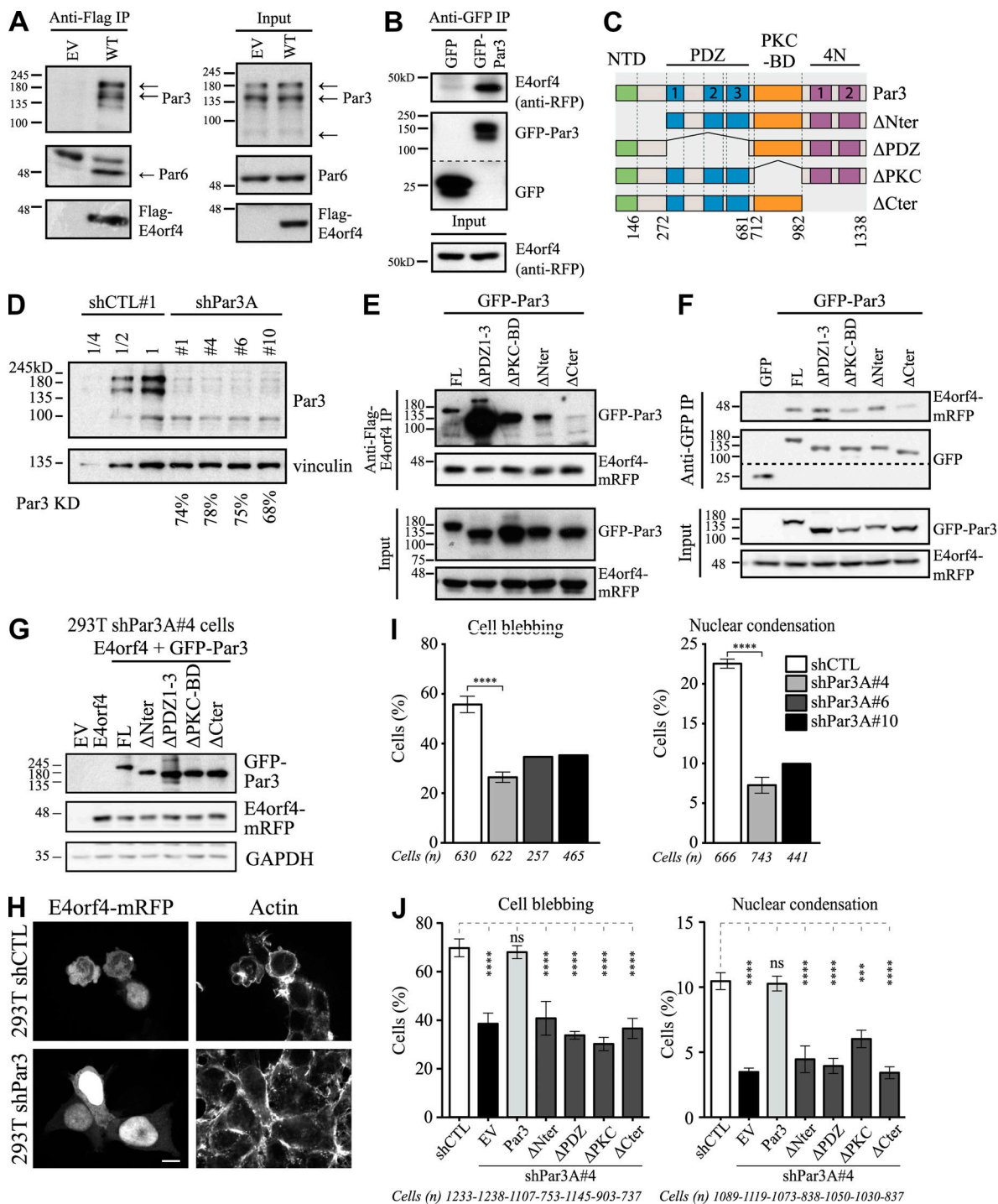


Figure S2. **Structure-function analysis of Par3 requirement for E4orf4's toxicity in HEK 293T cells.** (A) Flag-E4orf4 IP prepared from 293T cells transfected with the vector (EV) or Flag-E4orf4-mRFP, followed by IB for Par3 isoforms (arrows), and Par6; the levels of Flag-E4orf4 and Par6 in total cell extracts (Input), and GAPDH as a loading control, are shown. (B) GFP and GFP-Par3 IPs prepared from 293T cells transfected with E4orf4-mRFP together with GFP or GFP-Par3, followed by IB for the indicated antibodies; E4orf4 levels in total cell extracts are shown (Input). (C) Schematic representation of Par3-GFP proteins with functional domain deletions. (D) Representative IB showing the efficiency of Par3 depletion in 293T-shPar3 cell lines, estimated by loading increasing amounts of control cell extracts; vinculin is shown as a loading control. (E and F) Flag-E4orf4 IPs, or GFP-Par3 IPs, prepared from 293T-shPar3A#4 cells transfected with Flag-E4orf4-mRFP and GFP-Par3 constructs, followed by IB with the indicated antibodies; FL, full length GFP-Par3; $n > 2$; levels of E4orf4-mRFP and GFP-Par3 in total cell extracts are shown (Input). (G) IB showing the levels of GFP-Par3 proteins from a representative depletion-rescue experiment; GAPDH is shown as loading control. (H) Confocal images of 293T-shCTL and 293T-shPar3A#4 cells transfected with E4orf4-mRFP showing loss of E4orf4-dependent cell blebbing in Par3-depleted cells; F-actin is stained with phalloidin. Bar: 10 μm. (I) Quantification of the percentage of cell blebbing and nuclear condensation cells, as scored relative to cells expressing E4orf4-mRFP 24 h post-transfection for the datasets represented in H; data are from one representative experiment, or means \pm SEM [$n = 3$]. (J) Functional analysis of the molecular requirements of Par3 for E4orf4-induced cell blebbing and nuclear condensation by depletion-rescue (means \pm SEM [$n \geq 737$ cells; $n \geq 4$]). ***, $P < 0.001$; ****, $P < 0.0001$; ns, not significant.

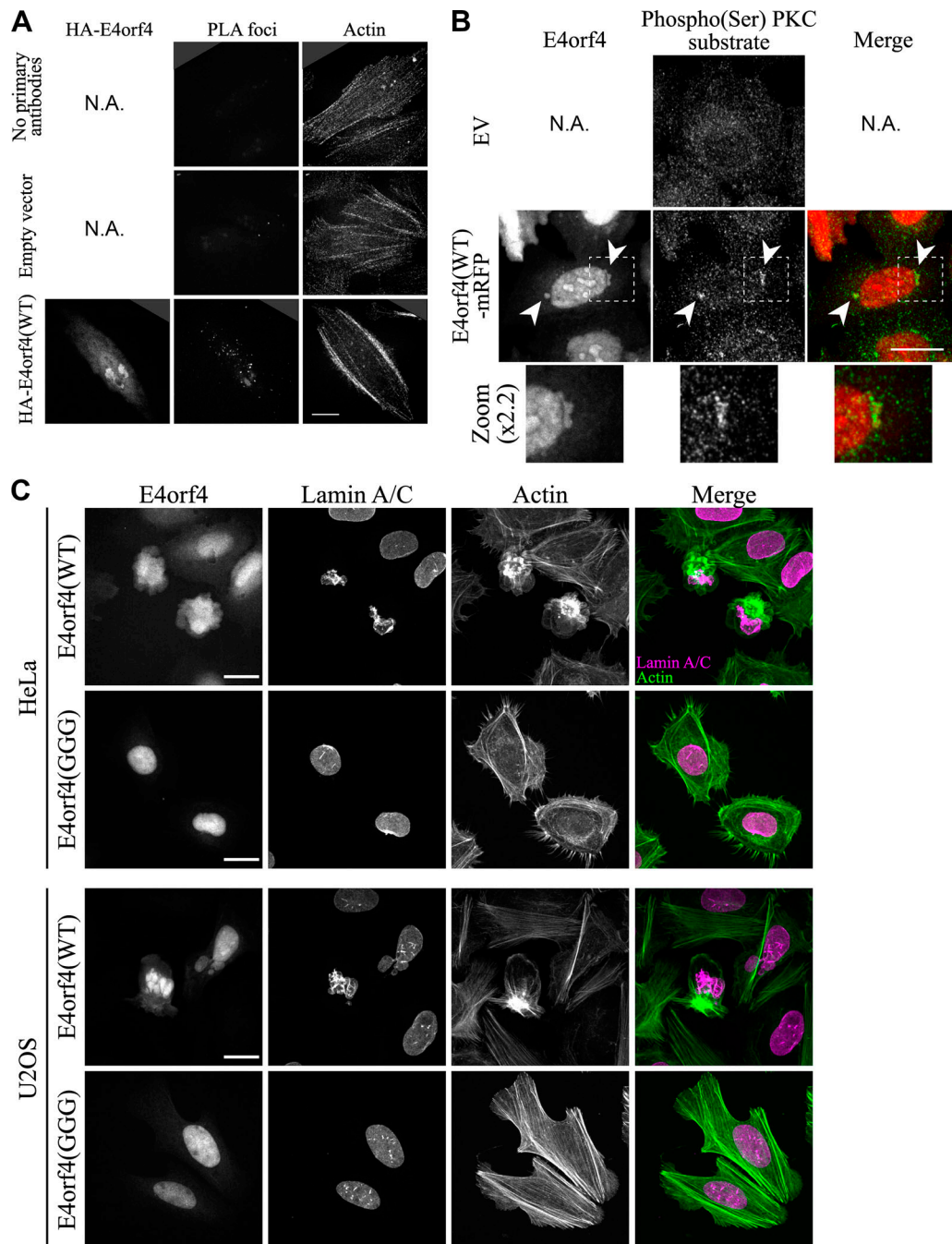


Figure S3. **Supporting information related to Fig. 4.** **(A)** Representative merged plane views from confocal image stacks of the PLA signal in controls, as detected when no primary antibodies are used (top row), or when cells are transfected with the empty vector instead of HA-E4orf4 (second row), as compared with the PLA reaction using anti-HA and anti-Par3 antibodies in cells transfected with HA-E4orf4 (third row); from $n = 3$. Bar: 20 μm . **(B)** Single plane confocal images of HeLa cells transfected with the empty vector (EV) or Flag-E4orf4-mRFP showing immunostaining of Ser-phosphorylated PKC substrates (in green). Enlarged views of the boxed regions emphasize positive clusters of PKC substrates designated by the arrowheads that are localized next to nuclear blebs. Bar: 20 μm ; N.A., not applicable **(C)** Maximum intensity projections of confocal image stacks of HeLa and U2OS cells showing the loss of tumoricidal phenotypes (cell blebbing and nuclear condensation-deformation) in cells expressing E4orf4 (GGG) as compared with cells expressing E4orf4 (WT); actin staining (green) and lamin A/C staining (magenta) are shown (representative of $n \geq 3$); bars, 20 μm .

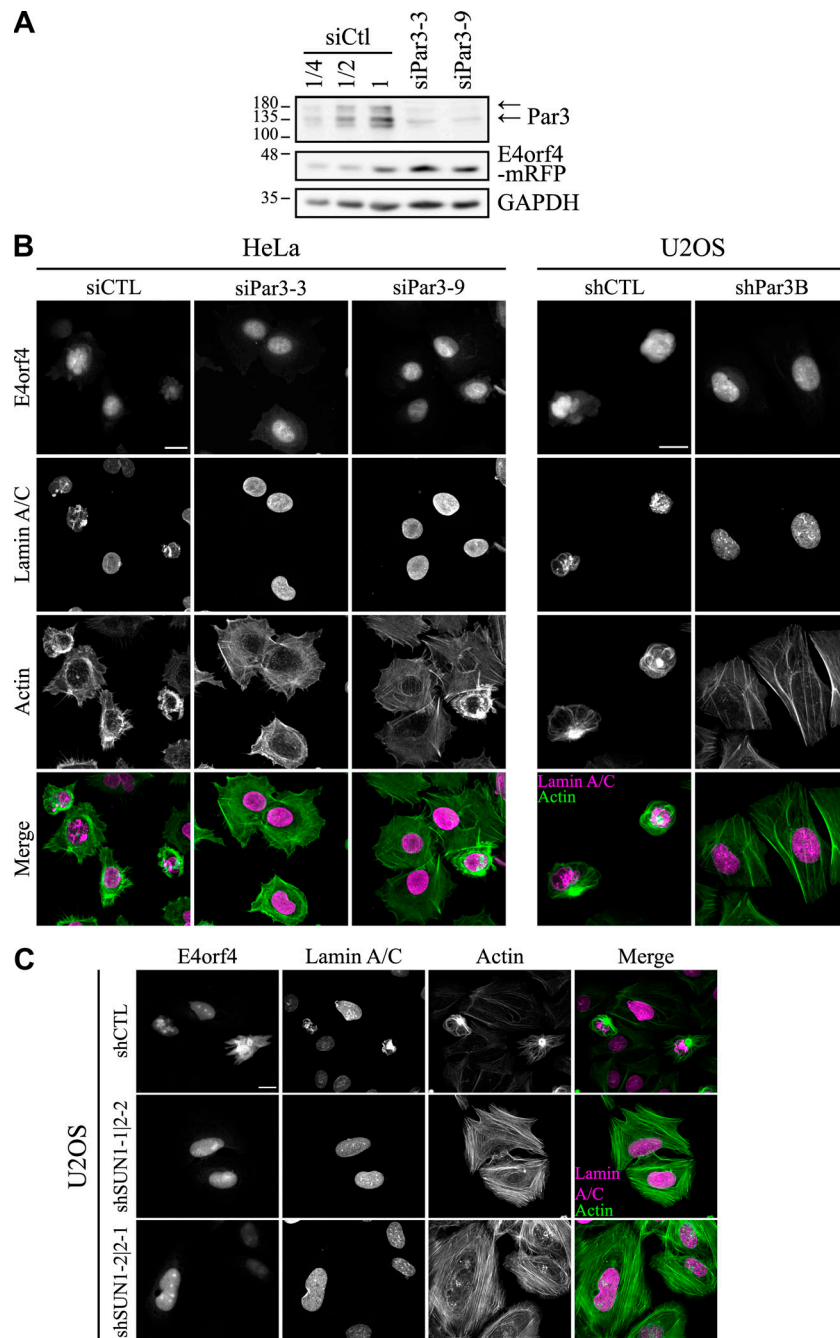


Figure S4. **Par3 depletion, as SUN1/2 depletion, impairs E4orf4 tumoricidal phenotypes.** (A) Representative IB of Par3 depletion in E4orf4-expressing HeLa cells (siPar3-3 and 3-9), as estimated by loading increasing amounts of control extracts (siCTL, 1, 1/2, and 1/4); GAPDH: loading control. (B and C) Maximum intensity projections of confocal image stacks of control E4orf4-mCherry-expressing HeLa or U2OS cells (siCTL and shCTL), as compared with cells treated with Par3-specific siRNAs (B), or transduced with lentivirus carrying Par3-specific shRNAs (B) or a mixture of SUN1/2-specific shRNAs (C), showing representative phenotypes. Please note that Par3 depletion, as SUN1/2 depletion, inhibited cell blebbing and nuclear condensation/dysmorphia; F-actin staining, green; lamin A/C staining, magenta. Bars: 20 μ m; $n \geq 3$.

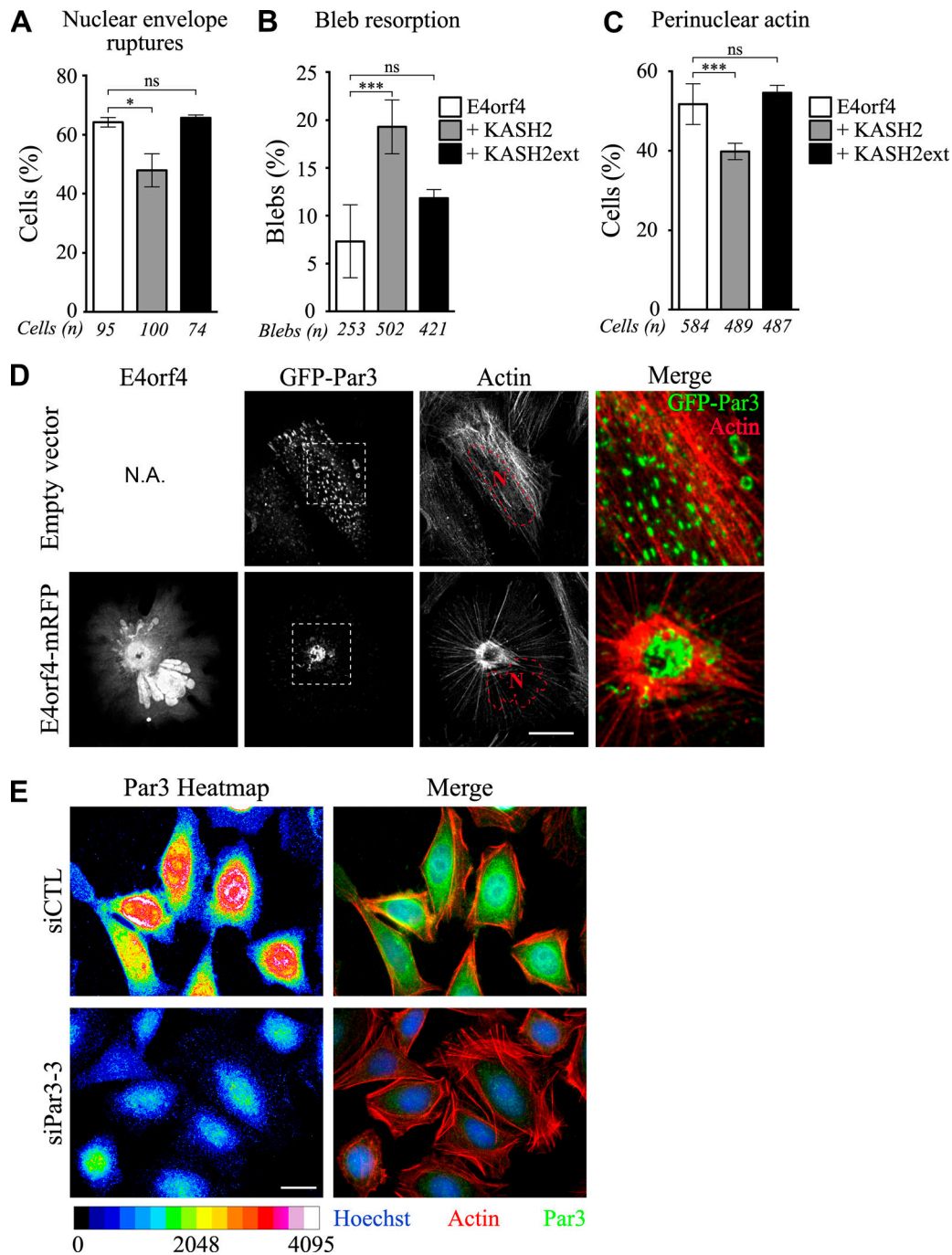


Figure S5. **Supporting information related to Fig. 7 and Fig. 8.** **(A)** The percentage of NE rupture after transfection with the vector, a dominant-negative KASH2 or an inactive KASH2ext, as scored relative to E4orf4-mRFP-expressing HeLa cells (means \pm SEM; $n \geq 3$). **(B)** The percentage of resorbing blebs in cells treated as in A, as scored relative to the total number of recorded blebs in E4orf4-mRFP-expressing HeLa cells, from an 8-h live-cell imaging performed 9 h after transfection (means \pm SEM; $n \geq 4$). **(C)** The percentage perinuclear actin remodeling in HeLa cells treated as in A, as scored by actin ring formation relative to E4orf4-mRFP-expressing cells 24 h after transfection (means \pm SEM, $n = 3$). **(D)** Representative deconvolved single plane confocal images of HeLa cells transfected with GFP-Par3 alone or E4orf4-mRFP; actin was stained with phalloidin. Red dotted lines outline nuclear shape (N), and enlarged views of the boxed regions show Par3-GFP distribution (in green) relative to F-actin organization in the perinuclear region (in red). Bar: 20 μ m. **(E)** Representative epifluorescence images of cells treated with siPar3-3 showing Par3 depletion efficiency in single cells. A heatmap was applied to show the reduction of Par3 signal. Bar: 20 μ m. *, $P < 0.05$; ***, $P < 0.001$; ****, $P < 0.0001$; ns, not significant.

Video 1. **E4orf4-induced nuclear bleb rupture, as compared with nuclear bleb resorption after Par3 depletion; related to Fig. 6 D.** Video microscopy of representative E4orf4-mRFP-expressing HeLa cells transfected with control (siCTL; left movie), or Par3-specific siRNA (siPar3-3; right movie). Cell imaging was performed after release from a 2-h blebbistatin treatment for a 3-h period at 90-s intervals using a PerkinElmer UltraVIEW spinning disk confocal equipped with CO₂/thermoregulated chamber and 40× 0.75 NA objective. Single-plane images are displayed at five frames/s.

Video 2. **Nuclear expression of mRFP alone does not induce nuclear bleb formation; related to Fig. 6.** Video microscopy of representative HeLa cells expressing mRFP-NLS. Cells were imaged for a 12-h period at 5-min intervals using a PerkinElmer UltraVIEW spinning disk confocal equipped with CO₂/thermoregulated chamber and 40× 0.75 NA objective; single-plane images are displayed at five frames/s.

Video 3. **E4orf4 induces nuclear bleb formation and rupture in U2OS cells; related to Fig. 6 G.** Video microscopy of a representative E4orf4-mCherry-expressing U2OS cell; a heatmap pseudo-color intensity scale was used to show E4orf4-mCherry signal, emphasizing nuclear E4orf4 efflux due to bleb rupture. Live-cell imaging was performed for an 8-h period at 5-min intervals using a PerkinElmer UltraVIEW spinning disk confocal equipped with CO₂/thermo-regulated chamber and 20× 0.50 NA objective; single-plane images are displayed at five frames/s.

Video 4. **E4orf4 induces repetitive nuclear bleb formation and rupture in MDA-MB-468 cells associated with a loss of NE integrity; related to Fig. 6 G.** Video microscopy of a representative E4orf4-mCherry-expressing MDA-MB-468 cell (cell in the center); a heatmap pseudo-color intensity scale was used to show E4orf4-mCherry signal and nuclear E4orf4 efflux due to bleb rupture. Cells were imaged for a 12-h period at 5-min intervals using a PerkinElmer UltraVIEW spinning disk confocal equipped with CO₂/thermoregulated chamber and 40× 0.75 NA objective; single-plane images are displayed at 10 frames/s.

Video 5. **E4orf4 triggers NE rupture/repair in HeLa cells; related to Fig. 7 A.** Video microscopy of a representative HeLa cell expressing GFP-NLS (gray) and Flag-E4orf4-mRFP (magenta). Cell imaging was performed for an 8-h period at 5-min intervals using a PerkinElmer UltraVIEW spinning disk confocal equipped with CO₂/thermoregulated chamber and 40× 0.75 NA objective; single-plane images are displayed at five frames/s.

Video 6. **E4orf4 triggers repetitive NE rupture/repair and loss of NE integrity in U2OS cells; related to Fig. 7 C.** Video microscopy of representative U2OS cells expressing GFP-NLS (gray) and Flag-E4orf4-mCherry (magenta); a cell undergoes repetitive cycles of NE rupture/repair associated with pronounced nuclear deformation (top cell), and another cell shows repetitive NE rupture/repair followed by a prolonged loss of NE integrity that is associated with intense cytoplasmic E4orf4 fluorescence and cell blebbing (bottom cell). Cell imaging was performed for a 10-h period at 5-min intervals using a PerkinElmer UltraVIEW spinning disk confocal equipped with CO₂/thermoregulated chamber and 40× 0.75 NA objective; single-plane images are displayed at five frames/s.

Video 7. **Retrograde movement of actin filaments toward the nucleus correlates with nuclear bleb formation and collapse; related to Fig. 9 A.** Video microscopy of a representative control U2OS cell expressing Flag-E4orf4-mCherry (magenta) and GFP-LifeAct (green) transfected with siCTL. Cell imaging was performed for an 8-h period at 5-min intervals, and confocal Z-stacks were acquired at 0.5- μ m steps using a PerkinElmer UltraVIEW spinning disk confocal equipped with CO₂/thermoregulated chamber and 40× oil 1.3 NA objective; maximum intensity projections of confocal image stacks are displayed at five frames/s.

Video 8. **Par3 depletion disrupts the directional and retrograde movement of actin filaments associated with nuclear bleb rupture; related to Fig. 9 A.** Video microscopy of a representative U2OS cell expressing Flag-E4orf4-mCherry (magenta) and GFP-LifeAct (green) transfected with Par3-specific siRNA (siPar3-3). Cell imaging was performed for an 8-h period at 5-min intervals, and confocal Z-stacks were acquired at 0.5- μ m steps using a PerkinElmer UltraVIEW spinning disk confocal equipped with CO₂/thermoregulated chamber and 40× oil 1.3 NA objective; maximum intensity projections of confocal image stacks are displayed at five frames/s.

Video 9. **E4orf4 induces a retrograde movement of actin filaments that correlates with nuclear deformation, nuclear bleb rupture, and loss of NE integrity; related to Fig. 9 D.** Video microscopy of representative control U2OS cells expressing Flag-E4orf4-mCherry (magenta) and GFP-LifeAct (green) transfected with siCTL. Cell imaging was performed for an 8-h period at 5-min intervals, and confocal Z-stacks were acquired at 0.5- μ m steps using a PerkinElmer UltraVIEW spinning disk confocal equipped with CO₂/thermoregulated chamber and 40× oil 1.3 NA objective; maximum intensity projections of confocal image stacks are displayed at five frames/s. Please note the NE integrity loss associated with a loss of E4orf4 compartmentalization in the bottom cell.

Video 10. **Transient NE rupture after depletion of lamins in HeLa cells; related to Fig 10 A.** Video microscopy of a representative mRFP-NLS-expressing HeLa cell transfected with a mixture of lamin A- and lamin B1-specific siRNAs. Cell imaging was performed for a 12-h period at 5-min intervals using a PerkinElmer UltraVIEW spinning disk confocal equipped with CO₂/thermoregulated chamber and 40× 0.75 NA objective; single plane images are displayed at five frames/s.